ORCA – Online Research @ Cardiff

This is an Open Access document downloaded from ORCA, Cardiff University's institutional repository:https://orca.cardiff.ac.uk/id/eprint/166106/

This is the author's version of a work that was submitted to / accepted for publication.

Citation for final published version:

Hogarth, L. M., Saintonge, A., Davis, T. A. , Ellison, L. S., Lin, L., Lopez-Coba, C., Pan, H.-A. and Thorp, M. D. 2024. The ALMaQUEST Survey XIV: do radial molecular gas flows affect the star-forming ability of barred galaxies? Monthly Notices of the Royal Astronomical Society 10.1093/mnras/stae377

Publishers page: https://doi.org/10.1093/mnras/stae377

Please note:
Changes made as a result of publishing processes such as copy-editing, formatting and page numbers may not be reflected in this version. For the definitive version of this publication, please refer to the published source. You are advised to consult the publisher's version if you wish to cite this paper.

This version is being made available in accordance with publisher policies. See http://orca.cf.ac.uk/policies.html for usage policies. Copyright and moral rights for publications made available in ORCA are retained by the copyright holders.

The ALMaQUEST Survey XIV: do radial molecular gas flows affect the star-forming ability of barred galaxies?

L. M. Hogarth[1]★, A. Saintonge[1]†, T. A. Davis[2], S. L. Ellison[3], L. Lin[4], C. López-Cobá[4], H.-A. Pan[5] and M. D. Thorp[6]

[1]*University College London, Department of Physics & Astronomy, Gower Street, London, WC1E 6BT, UK*
[2]*Cardiff Hub for Astrophysics Research & Technology, School of Physics & Astronomy, Cardiff University, Queens Buildings, Cardiff, CF24 3AA, UK*
[3]*Dept. of Physics & Astronomy, The University of Victoria, Victoria, BC V8P 5C2, Canada*
[4]*Institute of Astronomy & Astrophysics, Academia Sinica, No. 1, Section 4, Roosevelt Road, Taipei 10617, Taiwan*
[5]*Department of Physics, Tamkang University, No.151, Yingzhuan Road, Tamsui District, New Taipei City 251301, Taiwan*
[6]*Argelander-Institut für Astronomie, Universität Bonn, Auf dem Hügel 71, 53121 Bonn, Germany*

Accepted 2024 January 30. Received 2023 December 22; in original form 2023 September 1

ABSTRACT

We investigate whether barred galaxies are statistically more likely to harbour radial molecular gas flows and what effect those flows have on their global properties. Using 46 galaxies from the ALMA-MaNGA QUEnching and STar formation (ALMaQUEST) survey, we identify galaxies hosting optical bars using a combination of the morphological classifications in Galaxy Zoo 2 and HyperLEDA. In order to detect radial molecular gas flows, we employ full 3D kinematic modelling of the ALMaQUEST ^{12}CO(1-0) datacubes. By combining our bar classifications with our radial bar-flow detections, we find that galaxies classed as barred are statistically more likely to host large-scale radial gas motion compared to their un-barred and edge-on counterparts. Moreover, the majority of barred galaxies require multi-component surface brightness profiles in their best-fit model, indicative of the presence of a resonance system. We find that galaxies classed as barred with radial bar-flow ("barred + radial flow" subset) are significantly suppressed in global star-formation efficiency compared to barred galaxies without radial bar-flows and the other morphological sub-samples. Our "barred + radial flow" subset also possess consistently centrally concentrated molecular gas distributions, with no indication of depleted gas fractions, suggesting that gas exhaustion is not the cause of their suppressed star-formation. Furthermore, these objects have higher median gas densities in their central 1 kpc, implying that a central gas enhancement does not fuel a central starburst in these objects. We propose that dynamical effects, such as the shear caused by the large-scale inflow of gas, acts to gravitationally stabilise the inner gas reservoir.

Key words: galaxies: kinematics and dynamics – galaxies: structure – physical data and processes: molecular data

1 INTRODUCTION

Galactic bars are increasingly believed to be a critical stage in the secular evolution of disc galaxies in the present-day Universe (Masters et al. 2011; Chown et al. 2019; Géron et al. 2021, 2023). They provide an effective mechanism for the mass migration of molecular gas through instabilities driven by their axi-asymmetric structure. This process is well-understood and detailed in studies like Combes (1991); Bertin (2014); Sormani et al. (2015); Krumholz & Kruijssen (2015), which describe how bars exert powerful torques in their host galaxies that drive gas onto resonant orbits with epicyclic frequencies commensurate with the pattern frequency of the bar. This generally causes gas in the outer-disc to lose angular momentum and results in the formation of resonant ring structures in the host galaxy, with the strongest resonances being at co-rotation and at the Lindblad resonances (Shlosman et al. 1989; Combes 2001). Multiple direct observations of resonant ring structures using interferometry with high spatial resolution support these models (e.g. Olsson et al. 2010; Davis et al. 2018; Topal et al. 2016; Lu et al. 2022). However, observational studies with measurements directly capturing the radial motion of gas, as opposed to measurements of its spatial distribution, are more sparse. This is largely due to the resolution and sensitivity required to accurately separate non-circular gas motion from the rotation of the gas disc. With data

★ E-mail: l.hogarth.18@ucl.ac.uk
† E-mail: a.saintonge@ucl.ac.uk

© 2023 The Authors

that meets these criteria, the presence of non-circular kinematics is often estimated by assuming spectral components are Gaussian, and fitting asymmetric profiles as a superposition of Gaussians (e.g. Lu et al. 2022), but can also be inferred more comprehensively by full 3D kinematic modelling of the molecular gas (e.g. Lelli et al. 2022).

In reaction to the forcing frequency of a bar, simulations in the literature anticipate central starburst activity combined with quenching of the disc, resulting from the bulk inflow of molecular gas (e.g. Coelho & Gadotti 2011; Spinoso et al. 2017). Generally these simulations follow a "compaction scenario" (Tacchella et al. 2016), where galaxies cycle through active and passive star-forming phases, regulated by the inflow of molecular gas and subsequent outflow once intense star-formation is triggered. Tacchella et al. (2016) finds that galaxies at $z \sim 2$ will oscillate along the main-sequence on timescales $\approx 0.4\ t_H$ (where t_H is the Hubble Time). This scenario has also been simulated in the context of the Central Molecular Zone (CMZ) of a Milky Way-like galaxy by Krumholz & Kruijssen (2015). Their model predicts that the CMZ will cycle through phases above and below the star-forming main-sequence on a timescale of ~ 17.5 Myr at a resolution of ≈ 100 pc. The short timescales of star-formation and quiescence in this model are also in agreement with the observational study conducted by Ellison et al. (2011), who measure elevated chemical abundances in the centres of low-mass barred galaxies. This indicates that these galaxies have experienced some past central enhancement in their star-formation rates, which was short-lived compared to the lifetime of their bars.

However, there is some contention between observational studies that have found that bars can both suppress and enhance the star-formation efficiency (SFE) of their host galaxies. While multiple studies have confirmed elevated central molecular gas concentrations in barred galaxies (driven inwards by their forcing frequency at a rate faster than the gas is consumed e.g. Sakamoto et al. 1999; Jogee et al. 2005; Kuno et al. 2007; Yu et al. 2022), studies quantifying star-formation efficiency (SFE) are significantly more varied. Saintonge et al. (2012), for example, find no significant difference in the global SFE of barred galaxies compared to an un-barred sample. They acknowledge, however, that they may be averaging over galaxies undergoing different kinematic processes. This is reinforced by Jogee et al. (2005), who suggest that the SFE of barred galaxies varies depending on the stage of their bar-driven gas inflow; that only galaxies hosting later-stage flows, once most molecular gas has been driven into the circumnuclear region, have enhanced SFE compared to the mean. Studies such as Heitsch et al. (2006); Kruijssen et al. (2014); Davis et al. (2014); Meidt et al. (2020), however, have shown that strong non-circular motions stabilise molecular clouds against collapse or disperse them entirely, especially in the dense circumnuclear regions of galaxies. In the context of bars, suppression of SFE has been directly observed (e.g. Egusa et al. 2018; Maeda et al. 2020; Maeda 2023), but conversely, star-formation enhancement in the bar and circumnuclear region has also been reported (e.g. Watanabe et al. 2011; Wang et al. 2012; Salak et al. 2017), potentially reflecting the need to sub-divide barred galaxies based on their kinematic phase as suggested by Jogee et al. (2005); Saintonge et al. (2012).

In this study, we search for evidence of the effect optical bars have on the motion, distribution, and star-formation efficiency of molecular gas across a sample of nearby galaxies. More specifically, we seek to answer the following two questions:

1. Can we find a statistical relationship between the presence of an optical bar and the detection of radial molecular gas motion?
2. How does the detection of non-circular molecular gas motion influence the SFE of barred galaxies and their global properties?

By attempting to answer these questions, we aim to provide the kinematic counterpart to the spatial observations made of molecular gas distributions in barred galaxies. Furthermore, we want to address the conflicting conclusions in the literature as to whether a bar suppresses or enhances SFE in its host galaxy. We will address this by studying how ongoing radial gas motion impacts star formation activity, and how that relates to a galaxy's position on the star-forming main-sequence.

Throughout this paper we adopt a standard ΛCDM cosmology with $H_0 = 70$ km s^{-1} Mpc^{-1}, $\Omega_{m_0} = 0.3$, $\Omega_\Lambda = 0.7$ and a Chabrier (2003) IMF.

2 SAMPLE SELECTION & DATA

2.1 ALMaQUEST

The *ALMA-MaNGA QUEnching and STar formation* (ALMaQUEST) survey (Lin et al. 2020, ; Ellison et al. in prep.) consists of 47 galaxies selected from DR14 & DR15 of the *Mapping Nearby Galaxies at APO* (Apache Point Observatory) survey (MaNGA, Bundy et al. 2015), which span a wide range of specific star-formation rates and with stellar masses in the range $10 \lessapprox \log(M_*/M_\odot) \lessapprox 11.5$ (including the green valley, main-sequence and into the starburst regime; see Figure 1). *Atacama Large Millimeter/sub-millimeter Array* (ALMA) ^{12}CO(1-0) (rest frequency 115.271204 GHz) were collected from four individual ALMA observations: 2015.1.01225.S, 2017.1.01093.S, 2018.1.00558.S (PIs: Lin), and 2018.1.00541.S (PI: Ellison). We note that 1 object in the sample has no CO(1-0) detection.

All ALMA observations were taken in C43-2 configuration (synthesized beam 2.5″) to be comparable to the resolution of the optical integral field spectroscopy data from the MaNGA survey. Typically, ALMaQUEST data is spatially resolved on physical scales ≈1.5 kpc (ranging between 0.9 kpc to 6 kpc across the sample), with the largest structure the data is sensitive to being ≈14 kpc. The spectral setup includes a high-resolution spectral window with a channel width of ≈ 10 kms^{-1} targeting ^{12}CO$(1-0)$. The integration time for objects ranges from 0.2 – 2.5 hours to ensure a signal-to-noise greater than 3 for more than 50% of spatial pixels (spaxels) where the MaNGA Hα signal-to-noise is also greater than 3.

In order to generate moment maps and calculate total H2 masses we mask the ^{12}CO(1-0) datacubes by smoothing the original datacubes with a Gaussian kernel with a width of $1.5 \times \mathrm{Bmaj_{pix}}$ spaxels spatially (where $\mathrm{Bmaj_{pix}}$ is the width of the ALMA beam's major axes in pixels) and 4 channels spectrally. Values lower than the standard deviation of the original datacube are set to = 0 and all those above are set to = 1. The original datacubes multiplied by these masks are what we use to calculate the total CO(1-0) luminosity (L_{CO}) with the relation:

$$L_{CO} = 3.25 \times 10^7 \times S_{CO}\Delta v \times \nu_{sys}{}^{-2} \times D_L{}^2 \times (1+z)^{-3}\ , \qquad (1)$$

where S_{CO} is the total CO intensity obtained by summing over the masking cubes, Δv is the channel width, ν_{sys} is the systematic frequency of the CO(1-0) line, D_L is the luminosity distance and z is the redshift of the object (obtained from the NSA catalogue). The total gas mass for each object is then calculated using the constant Galactic conversion factor $\alpha_{CO} = 4.3\ M_\odot(\mathrm{K\ km\ s^{-1}\ pc^2})^{-1}$ since all the galaxies in the sample have near-solar metallicity (the median

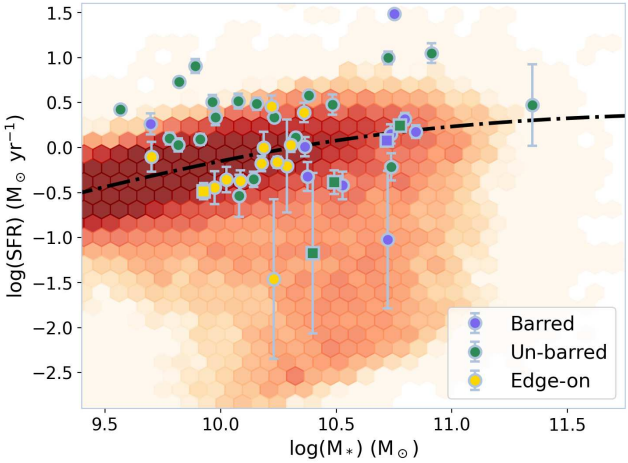

Figure 1. SFR-M$_*$ plot illustrating the position of the ALMaQUEST sample with respect to the star-forming main-sequence. SFRs are taken from the GSWLC-X2 catalogue (Salim et al. 2016, 2018) where available and stellar masses are taken from the NSA catalogue (Blanton & Roweis 2007; Blanton et al. 2011). The five objects not covered by GSWLC (square markers) are supplemented with SFRs from WISE (Wright et al. 2010). The GSWLC-X2 catalogue between $0.01 \leq z \leq 0.05$ is also illustrated in its entirety as a heat map and the star-forming main-sequence (as derived by Saintonge & Catinella 2022) is given as a black dashed line in the figure. We colour the markers by their morphological class ("barred", "un-barred" or "edge-on"). Our classification procedure is detailed in Section 2.3.

gas-phase metalllicity for ALMaQUEST objects is 8.69 ± 0.05) using values calculated in Lin et al. (2020) (with the O3N2 calibrator derived by Pettini & Pagel 2004).

2.2 Star-formation rates & stellar masses

2.2.1 *MaNGA data products*

As referred to in Section 2.1, the MaNGA survey (Bundy et al. 2015) is composed of integral field spectroscopic (IFS) observations of galaxies in the local Universe ($z \lesssim 0.15$) with coverage from 3600 Å to 10400 Å. We use optical emission line fluxes from the MaNGA Pipe3D pipeline derived from Data Release 17 (Sánchez et al. 2016, 2018; Sánchez et al. 2022). These are corrected for internal extinction by adopting an intrinsic Hα/Hβ = 2.86 and a Milky Way extinction curve (Cardelli et al. 1989). We follow the masking procedure detailed in Ellison et al. (2021), which makes restrictions on the optical spaxels used in their study combining MaNGA and ALMaQUEST data. This process can be summarised as follows:

1. Spaxels are required to have S/N > 2 in Hα, Hβ, [OIII]λ5007 and [NII]λ6584 maps.
2. Each spaxel must fall in the star-forming portion of the Baldwin, Phillips and Terlevich (BPT) diagram (Baldwin et al. 1981) using the Kauffmann et al. (2003) classification.
3. Spaxels require a Hα equivalent width (EW) > 6 Å.
4. Using stellar mass density maps (ΣM_*) from the Pipe3D pipeline, each spaxel must have $\log \Sigma M_* > 7$ (masking anomalously small values).

This procedure effectively masks low S/N spaxels and those contaminated by active galactic nuclei (AGN). We calculate star-formation rates (SFRs) from the extinction corrected, masked Hα maps using the relation given in Kennicutt (1998), so that:

$$\mathrm{SFR}\ [\mathrm{M_\odot yr^{-1}}] = 7.9 \times 10^{-42}\ \mathrm{L(H\alpha)}\ [\mathrm{ergs\ s^{-1}}]\ , \quad (2)$$

where L(Hα) is the luminosity of Hα emission. We note, however, that the masking process used to derive these SFR maps does significantly mask the central regions of some objects in the ALMaQUEST sample. In order to supplement MaNGA IFS, therefore, we also utilise independent global star-formation values (detailed in Sections 2.2.2 & 2.2.3).

2.2.2 *GSWLC*

The *GALEX-SDSS-WISE Legacy Catalogue* (GSWLC; Salim et al. 2016, 2018) contains measured properties for over 700,000 galaxies within the *Galaxy Evolution Explorer* (GALEX) footprint and with *Sloan Digital Sky Survey* (SDSS) redshifts between 0.01 and 0.3. The catalogue is split into two versions; GSWLC-1 and GSWLC-2. We use SFRs from GSWLC-X2, which use joint UV+optical+mid-IR SED fitting, using *Wide-field Infrared Survey Explorer* (WISE) 22 micron photometry (see Section 2.2.3).

GSWLC-X2 covers 41 of the 46 objects we use from ALMaQUEST and the values are illustrated in Figure 1 alongside the GSWLC-X2 catalogue between $0.01 \leq z \leq 0.05$.

2.2.3 *WISE*

For the remaining 5 objects from ALMaQUEST that are not included in the GSWLC-X2 catalogue, we use SFRs derived only from the WISE 22 micron photometry in the ALLWISE catalogue (Wright et al. 2010; Cutri et al. 2021). We employ the method outlined in Janowiecki et al. (2017) to calculate SFRs from W4 band fluxes ($\mathrm{SFR_{W4}}$), using SDSS redshifts to calculate luminosities of the W1 and W4 bands and use the calibration used by Jarrett et al. (2013) with a correction for stellar MIR contamination based on the W1 band luminosity:

$$\mathrm{SFR_{W4}}[\mathrm{M_\odot y^{-1}}] = 7.5 \times 10^{-10} \times (\mathrm{L_{W4}} - 0.044\mathrm{L_{W1}})[\mathrm{L_\odot}]\ , \quad (3)$$

where $\mathrm{L_{W1}}$ and $\mathrm{L_{W4}}$ are the W1 and W4 band luminosities respectively. We show the SFR values derived from WISE in Figure 1 alongside those from the GSWLC-X2 catalogue.

2.2.4 *NSA*

For all of our objects, we use stellar masses calculated from K-correction fit for Sersic fluxes from the *NASA-Sloan Atlas catalogue* (NSA; Blanton & Roweis 2007; Blanton et al. 2011). The NSA catalogue contains a wealth of fit parameters to photometry from local galaxies observed using the Sloan Digital Sky Survey (SDSS). We use the parameter `nsa_sersic_mass` from the `drpall-v3_1_1.fits` file released with DR17 of SDSS.

2.3 Morphological sub-samples

For this investigation, we require a robust method for identifying barred galaxies within the sample. To achieve this, we use two catalogues that contain morphological data; Galaxy Zoo Data Release 2 (GZ2; Willett et al. 2013) and HyperLEDA (comprised of the HyperCat and *Lyon-Meudon Extragalactic Database*/LEDA, henceforth

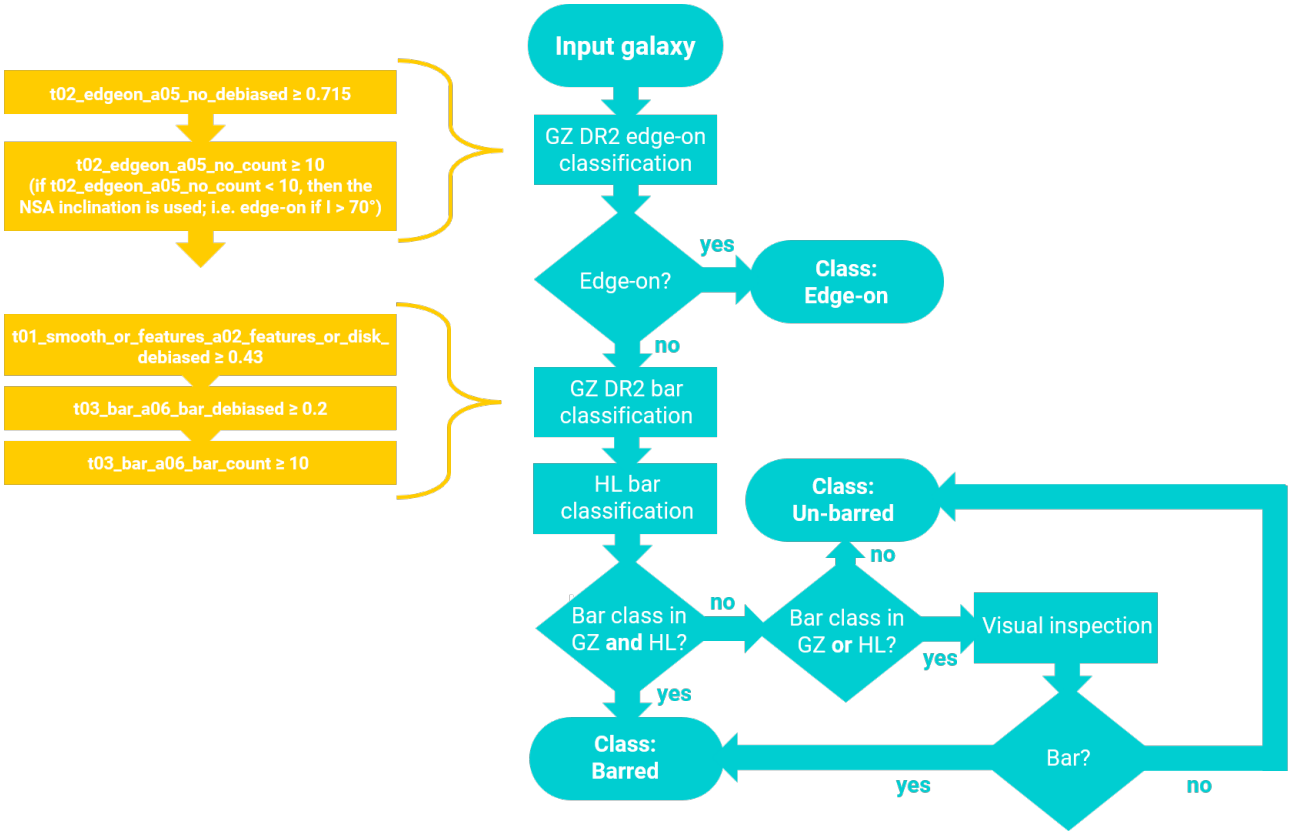

Figure 2. Flowchart illustrating our bar classification process using both Galaxy Zoo Data Release 2 (GZ2, Willett et al. 2013) and HyperLEDA (HL, Makarov et al. 2014).

referred to as HL; Makarov et al. 2014). We define three morphological sub-samples; "Barred", "Un-barred" and "Edge-on" (where "Edge-on" galaxies are too highly inclined to observe whether a bar is present). All galaxies in our sample are included in the HL database, but 5 are missing from GZ2. The procedure we devised using GZ2 and HL is illustrated as a flowchart in Figure 2.

For each galaxy in the sample, we first use GZ2 to determine whether the galaxy is "Edge-on" (we use redshift debiased values from GZ2 throughout this procedure, as defined by Willett et al. 2013). We find using the GZ2 classifications for the "Edge-on" sub-sample more accurate than using an inclination cut as the classification is based on whether the galaxy features are visible to the participants. Applying an arbitrary inclination cut led to some galaxies being classified as "Edge-On" when their features were still discernible (e.g. a central bar was visible). Details of the combination of GZ2 parameters used in this classification are included in Figure 2. We require a lower count thresholds in the `t02_edgeon_a05_no_count` and `t03_bar_a06_bar_count` parameters than the recommendation (i.e. we use $\geq$ 10 instead of $\geq$ 20), as we find low count numbers for this parameters for many objects in the sample. However, after a visual assessment, we still find these classification reliable with the lower count threshold. If the count number <10 for the `t02_edgeon_a05_no_count`, we instead use an inclination cut of $> 70^{\circ}$ (where inclination values are taken from the NSA catalogue) to determine if a galaxy is "Edge-on". We also use the lower limit for `t03_bar_a06_bar_debiased` of ≥ 0.2, where (Willett et al. 2013) find ≤ 0.2 correlates strongly with galaxies classified as un-barred by the reference sources Nair & Abraham (2010); de Vaucouleurs et al. (1991). Moreover, this lower limit is less biased towards strongly barred galaxies (i.e. it is more sensitive to weakly barred objects).

If a galaxy is not classed as "Edge-on", we look at whether they are classed as having an optical bar in both the GZ2 and HL (details of the parameters used from GZ2 are given in Figure 2). If GZ2 and HL both agree that the galaxy has a bar, it is added to our "Barred" sub-sample. Likewise, if they both agree that the galaxy is un-barred, we add it to our "Un-barred" sub-sample. If there is a disagreement between the catalogues (or it is only present in one of the catalogues), we visually inspect the SDSS RGB image of the object and decide whether or not a bar is present. We note, however, that our classification procedure is contingent upon the visibility of features in SDSS imaging, which is dependent on both the redshift of galaxies and their size. Using redshift debiased classifications from GZ2 along with the lower-limit for bar classification should reduce this effect to some extent, but we are unable to discount it entirely given the imaging and studies available.

In total, 10 objects are included in the "Barred" sub-sample, 23 in the "Un-barred" sub-sample and 13 in the "Edge-on" sub-sample. These sub-samples are represented using SDSS *gri* composite images of the galaxies in Figure 4. From this analysis, we calculate a bar fraction of 0.30, where the bar fraction calculated for the whole GZ2 sample in Willett et al. (2013) is 0.35 (given that we add the additional requirement of bar-detection in HL, a lower bar fraction is expected). Furthermore, the ALMaQUEST sample also covers a different range of global properties (e.g. M_*, SFRs, sizes, etc.) compared to the full GZ2 sample. Our sub-samples are referred to as the "morphological sub-samples" throughout the rest of this text.

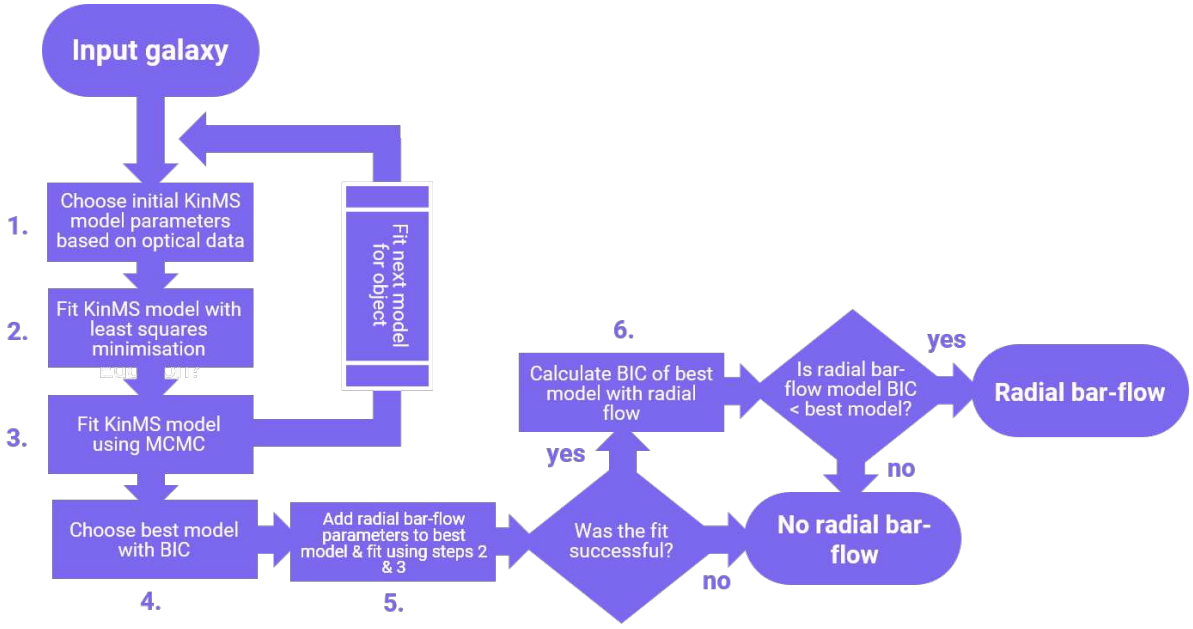

Figure 3. Flowchart illustrating our process for fitting and selecting the "best-fit" kinematic model for each of the galaxies in ALMaQUEST.

3 RESULTS

3.1 Kinematic models

In order to create three-dimensional kinematic models of the sample, we use the process described in Hogarth et al. (2023), which makes use of the KINematic Molecular Simulation tool (KinMS, see Davis et al. 2013; Davis et al. 2020; Lelli et al. 2022)[1,2]. KinMS allows us to create simple simulated interferometric data cubes by defining arbitrary surface-brightness and velocity profiles. We also use the `KinMS_fitter`[3] wrapper for KinMS, which acts as a front end for the most common fitting tasks, and provides a simple interface for defining surface brightness and velocity profiles. It also provides an interface to the GAStimator package[4], which implements a Python MCMC Gibbs-sampler with adaptive stepping employed to fit the mock interferometric data cubes generated by KinMS, with predefined surface-brightness and velocity profiles, to the original data cubes.

For each object in ALMaQUEST, we fit six different surface brightness profiles; an exponential disc, an exponential disc + central hole, a Gaussian ring, two exponential discs, an exponential disc + a Gaussian ring and two Gaussian rings (i.e. three single-component profiles and three double-component profiles). Each exponential disc has two free parameters describing the peak surface brightness ($F_{\rm exp,\ peak}$) and scale width ($R_{\rm exp}$), while each Gaussian ring has three free parameters describing the peak surface brightness ($F_{\rm gauss,\ peak}$), the mean radius of the ring ($M_{\rm gauss}$) and width of the ring ($\sigma_{\rm gauss}$). In order to reduce parameter numbers, in one-component models, the peak flux is fixed to =1 and in two-component profiles the peak flux of the first component in fixed to =1, while the others is left to vary relative to the first. In addition, each model has three parameters describing the kinematic centre of the gas disc; the spatial coordinates of the dynamic centre (x_0, y_0) and the systemic velocity $V_{\rm sys}$. Two further parameters, the position angle (PA) and inclination (i) are used to define the orientation of the disc. The total flux ($F_{\rm gas}$) contained in the disc is also left to vary freely. In all of the models we use an arctan velocity profile to capture the gas rotation, which we find an excellent approximation of the molecular gas rotation for the majority of the objects. This profile requires two additional parameters; the maximum velocity ($V_{\rm max}$) and the turnover radius ($R_{\rm turn}$; the radius at which $V_{\rm max}$ occurs), so that the rotation velocity ($V_{\rm rot}(r)$) is described by:

$$V_{\rm rot}(r) = \frac{2V_{\rm max}}{\pi} \arctan\left(\frac{r}{R_{\rm turn}}\right) \tag{4}$$

where r is the radius. The gas is also given a mean velocity dispersion ($\sigma_{\rm gas}$) in each model. The total number of parameters used in each model varies depending on the surface brightness model used, with 10 being the minimum and 14 the maximum.

In Figure 3, we illustrate the process we use to find the best-fit model for each of the objects in the sample. Before fitting each model with MCMC, we fit an initial model using a least squares minimisation. The MCMC is set with uniform priors with physically motivated boundaries and run using 100000 steps with 25 workers. Once a KinMS model has been fit using MCMC, we repeat steps 1-3 in Figure 3 until all six pre-defined models have been generated and fit to the data. When all models have been fit to the input galaxy, we use the Bayesian Information Criteria (BIC) to select the best-fit model from the six KinMS models. The best-fit model is the one that produces the lowest BIC value, where more complex surface brightness models will be penalised for larger parameter spaces so that:

$$\mathrm{BIC} = k\log(n) - 2\log(\widehat{L})\ , \tag{5}$$

where k is the number of parameters in the model, n is the number of spaxels in the datacube with signal and $\widehat{L}$ is the maximum value of the likelihood function defined in GAStimator. We reject

[1] https://github.com/TimothyADavis/KinMSpy
[2] https://kinms.space
[3] https://github.com/TimothyADavis/KinMS_fit
[4] https://github.com/TimothyADavis/GAStimator

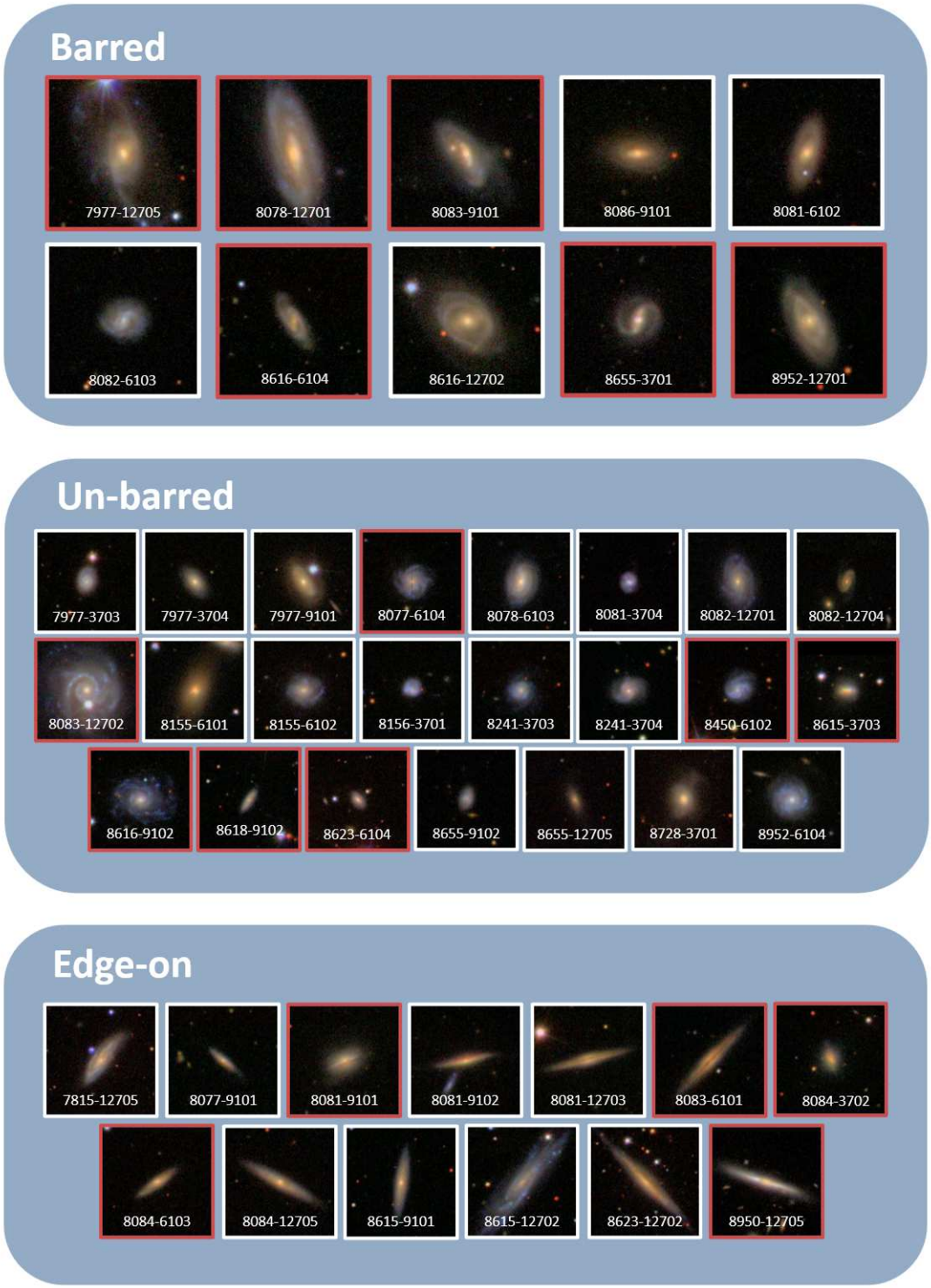

Figure 4. Optical SDSS gri composite images for each of the 46 galaxies in ALMaQUEST grouped by their morphological classification as detailed in Figure 2. Galaxies with a red border are classed as hosting radial bar-flows by the process described in Figure 3.

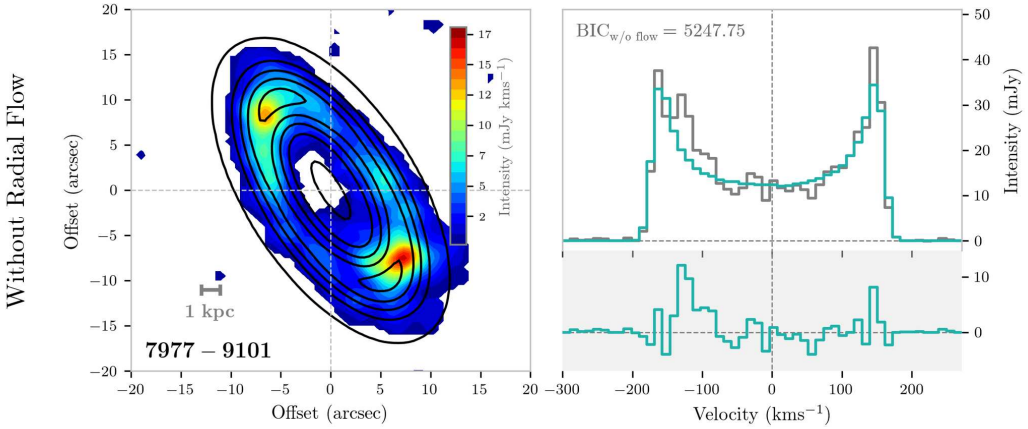

Figure 5. Example best-fit model for the ALMaQUEST galaxy with MaNGA Plate IFU 7977-9101 in our un-barred morphological sub-sample. **Left**: masked moment zero map of 7977-9101 with the best-fit model overlaid in black contours. **Right**: spectra extracted from the data cube for 7977-9101 (grey line) with the spectra extracted from the best-fit model cube (turquoise line). We also show the Bayesian Information Criteria (BIC$_{\rm w/o\ flow}$) for the model above the spectra. The lower panel shows the residual between the data and model spectra.

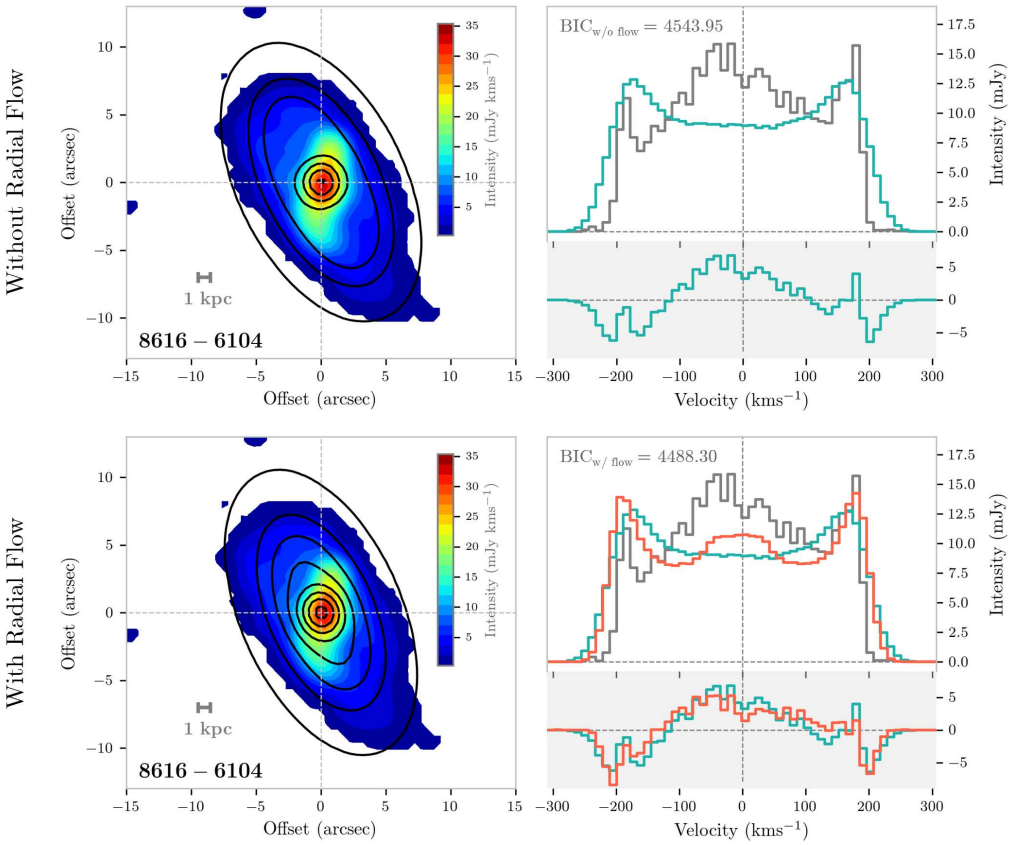

Figure 6. Example best-fit models for the ALMaQUEST galaxy with MaNGA Plate IFU 8616-6104 in our barred morphological sub-sample, without and with radial bar-flow (lower and upper figures respectively). The layout of the figures illustrated the two models is equivalent to that in Figure 5, except in the panel showing the spectra for the model with radial flow. In this panel, we plot the spectra extracted from the model without radial flow (turquoise) and from the model with radial flow (red) to aid a visual comparison between the two. We show the Bayesian Information Criteria for both models above the spectra (i.e. BIC$_{\rm w/o\ flow}$ and BIC$_{\rm w/\ flow}$). In the case of this object, BIC$_{\rm w/\ flow}$ < BIC$_{\rm w/o\ flow}$.

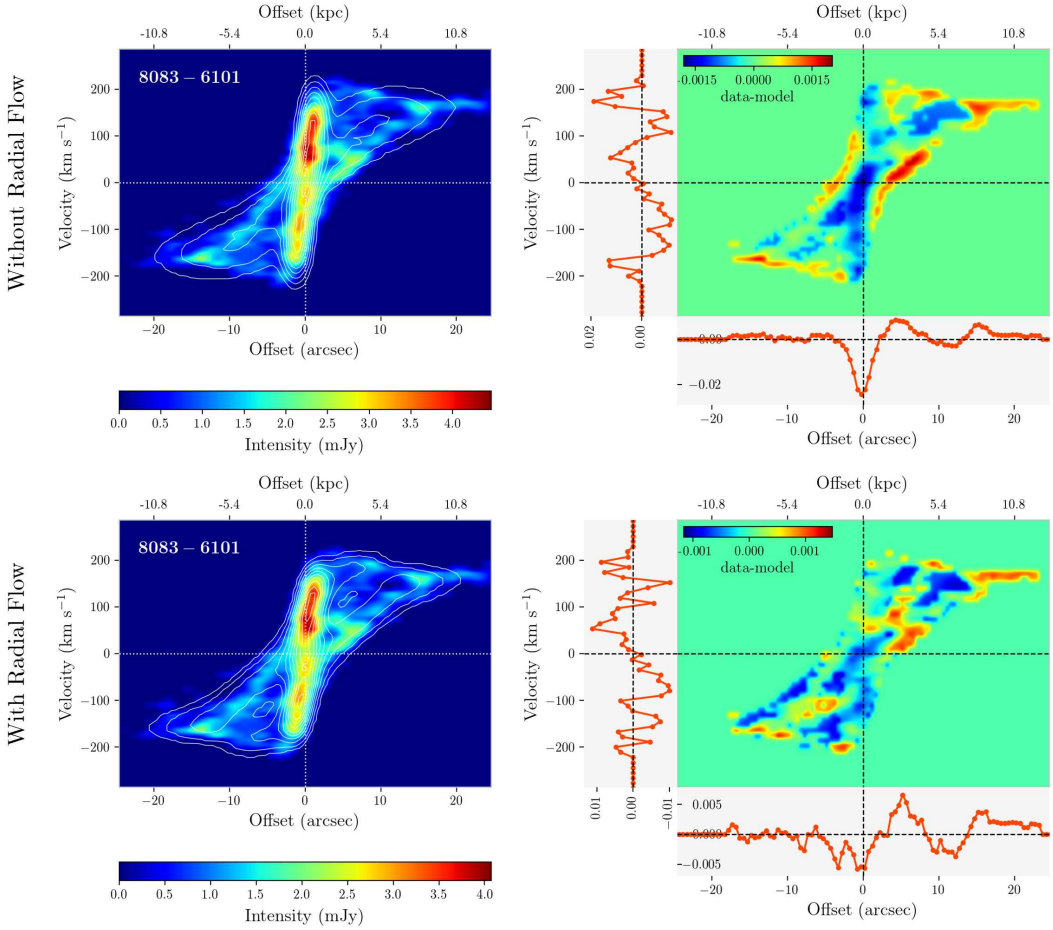

Figure 7. Example position-velocity diagrams (PVDs) illustrating the best-fit models for the ALMaQUEST galaxy with MaNGA Plate IFU 8083-6101 in our edge-on morphological sub-sample, both without and with radial flow included in the models (the upper and lower rows of figures respectively). **Left**: the PVD extracted form the original datacube for 8083-6101 is illustrated with a heatmap with the PVD extracted from the model overlaid as white contours. The kinematic centre (as determined by the model) is given by the white dashed lines. **Right**: The residual map calculated by subtracting the model PVD from the data PVD. One the left and bottom of this figure are the 1D residuals created by summing over the residual map in the offset and velocity axes respectively. The Bayesian Information Criteria (BIC) for the model with radial bar-flow (lower row) < than the model without radial bar-flow (upper row) for this object.

models that have fit parameters with uncertainties (defined as the width between the 16th and 84th) larger than half the size of the parameter space (we find this works well as a method of rejecting unconverged models). We successfully find a converged best-fit model for each object in the sample.

The next stage in our process is to add radial bar-flow to the best-fit model (again using the same technique outlined in Hogarth et al. 2023). We model radial motion induced by a central bar by using the `radial_barflow` function within the `KinMS_fitter` wrapper, which is based on the non-axisymmetric models described in Spekkens & Sellwood (2007). This radial bar-flow model simplifies the models outlined in Spekkens & Sellwood (2007) by assuming that there is a bar that extends from the galaxy's centre to a radius R_b, with a phase ϕ_b and that the gas has a constant radial and transverse velocity $(\overline{V}_r, \overline{V}_t)$ within the bar's radius. $\overline{V}_r$ represents the mean radial flow in the plane of the disc and $\overline{V}_t$ is the mean streaming speed of the gas perpendicular to $\overline{V}_r$. The total bar-flow velocity $(V_f(r,\theta))$ is defined as:

$$V_f(r,\theta) = \begin{cases} V_f(\theta), & \text{if } r \leq R_b \\ 0, & \text{if } r > R_b \end{cases} \tag{6}$$

where θ is the angle in the disc plane relative to the major axis and $V_f(\theta)$ is the bar-flow velocity at radii $\leq R_b$, which varies only with θ so that:

$$V_f(\theta) = -\sin i[\overline{V}_t \cos(2(\theta_b))\cos\theta + \overline{V}_r \sin(2(\theta_b))\sin\theta] \tag{7}$$

where $\theta_b = \theta - \phi_b$, representing the angle relative to the position angle of the bar. This simplified radial bar-flow model is a first-order approximation of the non-circular kinematics of gas in the presence of a bar, where we assume that the bulk of the flow will happen in the circumnuclear region of the galaxy and that the flow in this region can be described with constant $\overline{V}_t$ and $\overline{V}_r$ (i.e. without a radial dependence). This reduces computational time by reducing $V_f(r,\theta) \rightarrow V_f(\theta)$, and allows us to identify the presence of radial bar-flow statistically over a sample of galaxies.

The radial bar-flow approximation adds an additional four parameters to our models. At minimum, therefore, each model has 14 free parameters and at maximum 18 free parameters. For each galaxy, we re-fit our best-fit model with radial bar-flow using MCMC, using the same priors and setup as described previously (with additional uniform priors for the radial bar-flow parameters). If the model does not converge (based on the width of the parameter

uncertainty), we classify the object as not having radial bar-flow. We also require either the $\overline{V_t}$ or $\overline{V_r}$ to be larger than 2× the channel width ($2 \times \Delta_{\rm channel} \approx 22$ kms^{-1}) as a threshold for radial bar-flow detection. If these requirements are met, we re-calculate the BIC using the new model and parameter space in step 6 (see Figure 3) and if $\mathrm{BIC}_{\mathrm{w/\ radial\ flow}} < \mathrm{BIC}_{\mathrm{w/o\ radial\ flow}}$, it is classed as having radial bar-flow (otherwise, it is classed as not having radial bar-flow). We note that in the majority of our barred objects classed as hosting radial bar-flow, we find good visual alignment between the sky projection of ϕ_b and the optical position angle of the bar (echoing the results of López-Cobá et al. 2022, who find this result with more a detailed bisymmetric flow model).

In Figures 5, 6 & 7 we present examples of the models generated using the process detailed in Figure 3. Figure 5 illustrates the best-fit model for the object with MaNGA Plate IFU 7977-9101 in our un-barred sub-sample, which is a Gaussian ring with no radial bar-flow component (in this case, we did not find a model with radial bar-flow with a converged solution). In Figure 6, we show the models with and without radial bar-flow for object 8616-6104 in our barred sub-sample. This object has a more complex structure, and is best fit with a central exponential disc and outer Gaussian ring. Adding a radial bar-flow component also improves the fit to the data by lowering $\mathrm{BIC}_{\mathrm{w/o\ flow}} = 4543.95$ to $\mathrm{BIC}_{\mathrm{w/\ flow}} = 4488.30$. We overlay the spectra from the model with radial bar-flow over the model with no radial bar-flow in Figure 6 to illustrate the improvement.

In Figure 7, we present the position velocity diagrams (PVDs) extracted from the models both with and without radial bar-flow for object 8083-6101 in our edge-on sub-sample (we choose an edge-on object here as kinematic features are more easy to discern in objects that are more inclined). Again, the best-fit model for this object is determined to be two Gaussian rings with radial bar-flow. Both the shape of the PVD extracted from the model and the residual when compared to the data is improved by including radial bar-flow. In total, 19 objects in ALMaQUEST are classed as having radial bar-flow, which we will refer to as the "radial-flow subset" for the remainder of this paper. These subsets are also represented in Figure 4.

3.2 Statistical presence of radial bar-flows

Our first question, as laid out in Section 1, requires us to determine whether we see a statistical relationship between the presence of an optical bar and the detection of non-circular kinematics like radial bar-flow. In Figure 8, we show the proportion of galaxies in the radial bar-flow subset when divided into the morphological sub-samples. We find that 60% of the objects in the barred sub-sample are also in the radial bar-flow subset, compared to 30% and 38% in the un-barred and edge-on sub-samples respectively. It can be assumed that the edge-on sub-sample is composed of both barred and un-barred galaxies, so a radial bar-flow proportion that falls between that of the barred and un-barred sub-samples is consistent. With our bar fraction of 0.30, and given the radial bar-flow detection proportions in the barred and un-barred sub-samples, we would expect 39% of the edge-on sub-sample to be in the radial bar-flow subset, very close to our measured edge-on radial bar-flow fraction of 38%. For completion, we demonstrate the effect of small number statistics in Figure 8 by also giving the standard error for each morphological sub-sample, assuming a binomial distribution (i.e. error on each bar = $\sqrt{(p_{\mathrm{r,i}}\, p_{\mathrm{nr,i}})}\,/N_{\mathrm{morph,i}}$, where $N_{\mathrm{morph,i}}$ is the number of objects in each morphological sub-sample i, $p_{\mathrm{r,i}}$ is the radial bar-flow fraction and $p_{\mathrm{nr,i}}$ is the no radial bar-flow fraction).

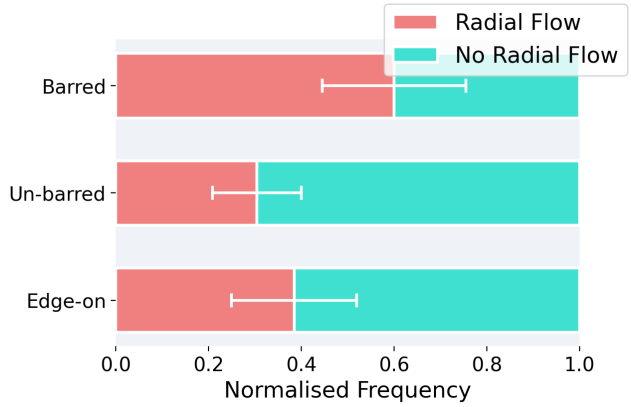

Figure 8. Bar plot representing the fraction of galaxies in each morphological sub-sample in ALMaQUEST that are determined to have radial bar-flow in their best-fit model. The frequency is normalised by the total number in each sub-sample for ease of comparison. 67% of the barred sub-sample are determined to have radial bar-flow, compared to 24% and 50% in the un-barred and edge-on sub-samples respectively. The errorbars represent the standard error on the radial bar-flow fraction for each of the morphological sub-samples assuming a binomial distribution.

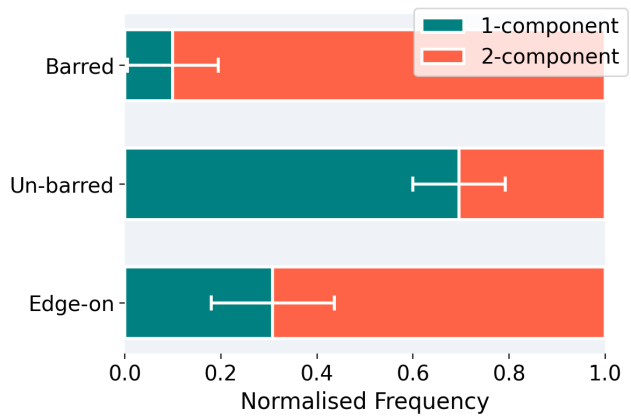

Figure 9. Bar plot representing the fraction of galaxies in each morphological sub-sample in ALMaQUEST that are determined to have a single component (1-component) or double component (2-component) surface brightness profile in their best-fit model (see Section 3.1 for more details). The frequency is normalised to the total number in each sub-sample for ease of comparison. 89% of the barred sub-sample are determined to have 2-component surface brightness models, compared to 40% and 58% in the un-barred and edge-on sub-samples respectively. The errorbars represent the standard error on the radial bar-flow fraction for each of the morphological sub-samples assuming a binomial distribution.

Our predicted fraction of edge-on galaxies with radial bar-flow (i.e. calculated from the bar fraction) is well within the uncertainty for this morphological sub-sample. We also note that radial kinematics are more easily identified in galaxies with a higher inclination, as the component of the motion projected along the line-of-sight with be higher. This could potentially increase the radial bar-flow proportion in the edge-on sub-sample, however, given how close our predicted radial bar-flow fraction for the edge-on sample (inferred from the barred and un-barred sub-samples) is to our measured value, this effect does not appear to be significant.

In Figure 9, we look at the proportion of galaxies that require a 1- or 2-component surface brightness model in their best-fit KinMS

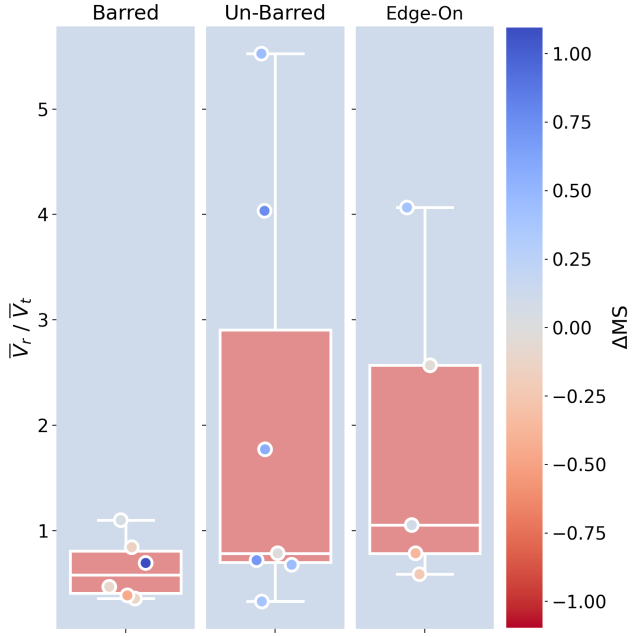

Figure 10. Distribution of the $\overline{V}_r/\overline{V}_t$ ratio (see text for definition) for each of the bar sub-samples. The sample is divided into the three morphological sub-samples in the panels in the figure. The median position, inner quartiles and span of the distributions are given by box plots in each of the three panels and the individual values given as markers. The markers are colour-coded by their SFR offset from the main-sequence (ΔMS).

model (see Section 3.1) for each morphological sub-sample. The top panel in the figure illustrates that the barred sub-sample is dominated by 2-component models (90%), compared to the un-barred and edge-on sub-samples (30% and 69% respectively). 2-component surface brightness models are generally associated with multiple gas rings, such as those caused by the forcing frequency of an axi-asymmetric feature like a bar. It follows, therefore, that our barred sub-sample would contain a high fraction of multiple-component models. We also anticipate that the fraction of barred sub-sample with multi-component models would be greater than the fraction of those with radial bar-flow, as flows are transient while the resonant structures exist over far longer timescales.

Using the objects in our radial bar-flow subset, in Figure 10 we look at the distribution of the ratio between the radial velocity component ($\overline{V}_r$) and the transverse velocity component ($\overline{V}_t$) of the radial bar-flow model (see Section 3.1). If $\overline{V}_r$ / $\overline{V}_t$ < 1, it suggests that the gas is more dominated by the transverse velocity component and, therefore, moving in a tighter "spiral motion" than if $\overline{V}_r$ / $\overline{V}_t$ > 1, which would indicate that the gas is moving more directly in the radial direction. In Figure 10, we observe that the $\overline{V}_r$ / $\overline{V}_t$ values in our barred sub-sample are all $\lesssim$ 1, whereas we see a greater spread of values in both the un-barred and edge-on sub-samples. This could imply that the un-barred and edge-on sub-samples contain objects undergoing a range of dynamical processes driving the flow of molecular gas, as opposed to the barred sub-sample where we see more consistency. We can infer from this that there may be a similar kinematic process driving the flow of gas in the barred sub-sample (i.e. the forcing frequency of a bar).

3.3 Effect of radial bar-flow on the global SFE of barred galaxies

Our second question posed in Section 1 involves investigating how non-circular molecular gas kinematics affects the global SFE of barred galaxies. We define the SFE as the ratio between total SFR (SFR_{tot}) and total H2 gas mass ($M_{H2,tot}$). The SFR_{tot} values we use are detailed in Sections 2.2.2 & 2.2.3 from the GSWLC-X2 and WISE catalogues, and we calculate $M_{H2,tot}$ using our masked ALMaQUEST ^{12}CO(1-0) datacubes (see Section 2.1).

In Figure 11 we plot the distribution of the quantity $\log(SFE_{measured}) - \log(SFE_{expected})$, which estimates the enhancement/suppression of SFE relative to what would be expected given an object's place on the main-sequence. $\log(SFE_{measured})$ are the SFE values we calculate with SFR_{tot} and $M_{H2,tot}$. $\log(SFE_{expected})$ is a function of the object's offset from the main-sequence ($\Delta MS(M_*)$), which we define as:

$$\Delta MS(M_*) = SFR_{tot} - SFR_{MS}(M_*) \,, \tag{8}$$

where $SFR_{MS}(M_*)$ is the main-sequence as a function of stellar mass (M_*) using the Saintonge & Catinella (2022) function, which is revised from the Saintonge et al. (2016) function by using M_* and SFR values from GSWLC-2:

$$SFR_{MS}(M_*) = 0.412 - \log\left(1 + \left[\frac{10^{M_*}}{10^{10.59}}\right]^{-0.718}\right) \tag{9}$$

We then derive $\log(SFE_{expected}(\Delta MS))$ by fitting a line to the $\Delta\log(SFE)$ values illustrated in Figure 9 of Saintonge & Catinella (2022) with the form:

$$SFE_{expected}(\Delta MS) = 0.29 \times \Delta MS + 0.04 + (-9.12) \,, \tag{10}$$

where -9.12 is the median value of log(SFE) for ALMaQUEST galaxies in the un-barred sub-sample that are ±0.3 dex from the star-forming main-sequence (this aids interpretation of the relative offset between samples with respect to un-barred main-sequence galaxies). Any enhancement/suppression in SFE measured for our barred sub-sample, therefore, may purely be a consequence of their place relative to the star-forming main-sequence. Equally, the presence of a bar could be driving the position of the galaxy on the main-sequence. For both scenarios, using $\log(SFE_{measured}) - \log(SFE_{expected})$ should reduce this effect.

In the left-side panel of Figure 11, we see an indication that the "barred + radial flow" subset has generally suppressed SFE, relative to both the "barred + no radial flow" subset and un-barred sub-sample. We note that these subsets are small, particularly the "barred + no radial flow" subset, so our analysis is once again limited by the small number of galaxies we are analysing in this work. However, we see a tenuous suggestion that the presence of a radial flow in barred galaxies suppresses their SFE relative to the "barred + no radial flow" subset and un-barred sub-sample. In the right-side panel of Figure 11, we plot the un-barred sub-sample alongside the "barred + radial flow" and "barred + no radial flow" subsets. We calculate the 2-sided Kolmogorov–Smirnov (KS) statistic for both radial flow barred subsets with the un-barred sub-sample and find that while the "barred + no radial flow" subset is likely drawn from the same distribution as the un-barred sub-sample, the p-value for the "barred + radial flow" subset is < 0.05. This implies that we can reject the null-hypothesis and the "barred + radial flow" subset is likely drawn from a different distribution to the un-barred sub-sample.

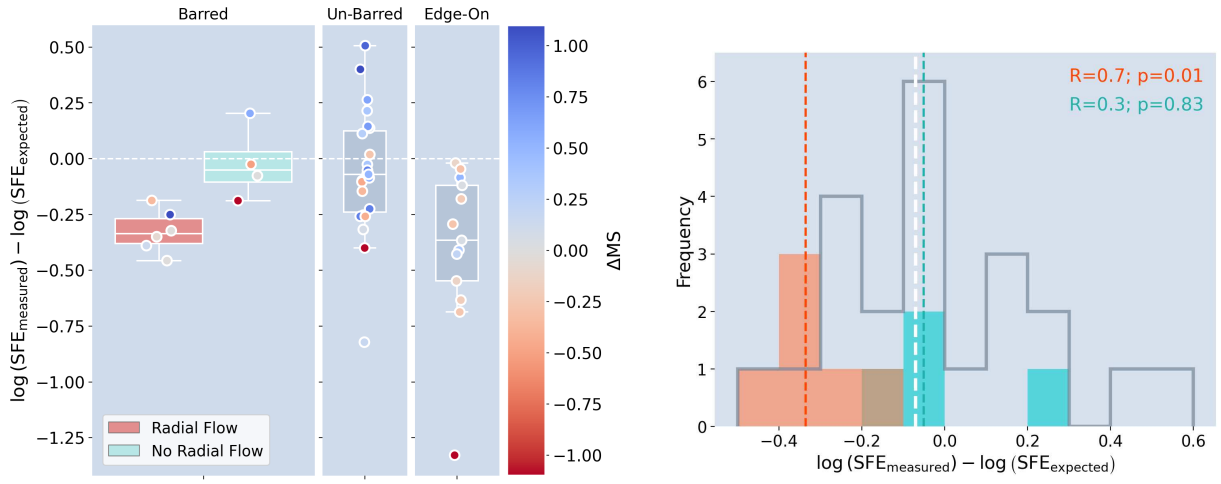

Figure 11. Figures illustrating the distribution of the $SFE_{measured} - SFE_{expected}$ quantity (see text for definition) for ALMaQUEST. **Left**: the sample is divided into the three morphological sub-samples in the panels in the figure as in Figure 10 and split in the barred panel into radial bar-flow subsets. The median position, inner quartiles and span of the distributions are given by box plots in each of the three panels and the individual values given as markers. The markers are colour-coded by their SFR offset from the main-sequence (ΔMS). **Right**: histograms illustrating the $SFE_{measured} - SFE_{expected}$ quantity for the un-barred sub-sample (grey "step" histogram) and the "barred + radial flow" and "barred + no radial flow" subsets (red and turquoise histograms respectively). The median position of each histogram is given by the white, red and turquoise dashed lines for the un-barred, "barred + radial flow" and "barred + no radial flow" distributions respectively. The 2-sided KS statistic and p-value are given in the plot to determine whether the "barred + radial flow" and "barred + no radial flow" distributions are drawn from the same distribution as that from the un-barred sub-sample. The p-value for the "barred + radial flow" subset suggests we can reject the null hypothesis, however, we note the low numbers in our statistic analysis.

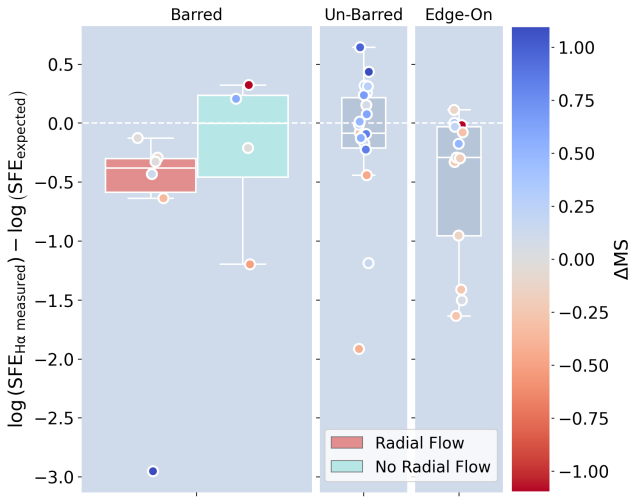

Figure 12. The distribution of the $SFE_{H\alpha,measured} - SFE_{expected}$ quantity (see text for definition) in the disc region of ALMaQUEST objects using Hα emission from MaNGA. For each object, we sum SFR and M_{H2} spaxels within a circular annulus between 1 kpc - $r_{50,r}$ in order to estimate the total disc SFE. The layout of this figure is equivalent to the lefthand plot in Figure 11.

Using SFR maps derived from Hα emission from MaNGA, in Figure 12 we plot the distribution of $SFE_{H\alpha,measured} - SFE_{expected}$ for the disc regions of the ALMaQUEST galaxies. We exclude the central region due to some objects (particularly in the barred sub-sample) having much of this area masked due to AGN-contamination or low-S/N. With the SFR maps calculated using the method detailed in Section 2.2.1, we estimate the total disc SFR by summing spaxels in a circular annulus between 1 kpc and the r-band effective radius from the NSA catalogue for each object ($r_{50,r}$). M_{H2} spaxels then are summed in the same region and used to calculate $SFE_{H\alpha,measured}$. The $SFE_{expected}$ values used are the same as those derived in Equations 8-10 using SFR_{tot} from GSWLC-X2 and WISE. We find a similar relative distribution between our morphological sub-samples as we observe in Figure 11. Again, we are limited in particular when we interpret differences between the radial subsets in this figure due to the size of the samples, but we do see an indication that the median value of the "barred + radial flow" distribution is suppressed relative to that of the "barred + no radial flow" subset, which is approximately coincident with that of the un-barred sub-sample (although there is significant scatter). Using the same method as in Figure 11, we use the 2-sided KS test to discern whether the SFE values from the radial bar-flow subsets in the barred sub-sample are drawn from the same distribution as the un-barred sub-sample. We find again that the p-value < 0.05 for the "barred + radial flow" subset but » 0.05 for the "barred + no radial flow" subset. This could imply that SFE is suppressed in the discs of galaxies in the "barred + radial flow" subset relative to those in the unbarred sub-sample, which may contribute to the variations in global SFE distributions that we observe in Figure 11. In the Appendix, we also attempt to observe differences in $SFE_{H\alpha,measured} - SFE_{expected}$ between our morphological sub-samples and radial flow subsets in the central 1 kpc using median SFE spaxel values available in this region.

We conduct a similar analysis to that carried out in Figure 11 in Figure 13, where we look at the distribution of concentration parameters for the objects in ALMaQUEST. The concentration parameter is defined as the half-light radius of the CO(1-0) intensity for each object, divided by $r_{50,r}$ (i.e. $r_{50,CO}/r_{50,r}$). In the left-side panel of Figure 13, we illustrate the distribution of concentration parameters for each of the morphological sub-samples and the barred radial bar-flow subsets. The objects in the "barred + radial flow" subset all fall below ≈ 0.4, whereas in the other morphological sub-samples there is a broader distribution of values. In the right-side panel of Figure 13, we compare the un-barred concentration parameter dis-

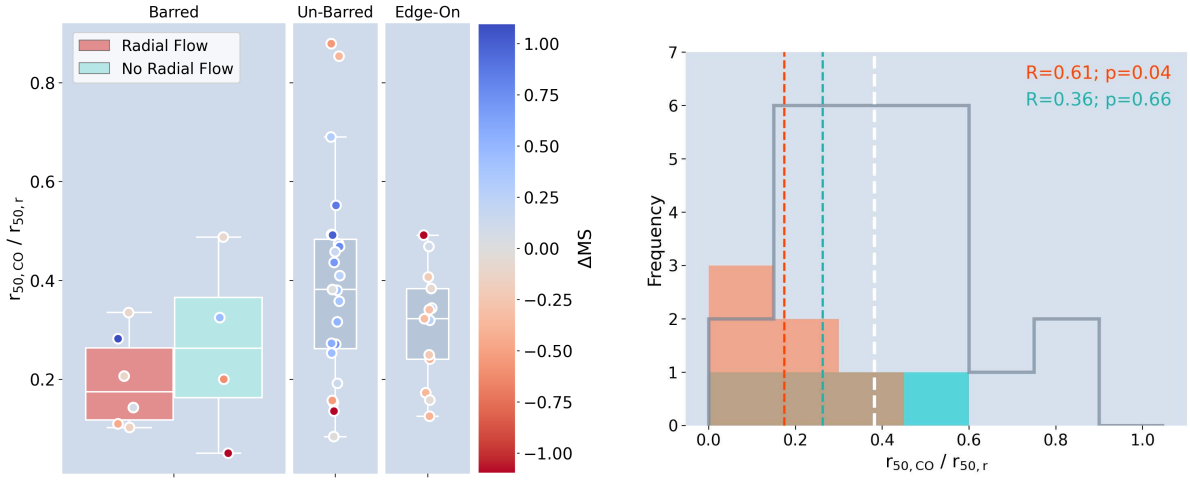

Figure 13. Figures illustrating the distribution of the concentration parameter ($r_{50,CO}/r_{50,r}$, see text for more details) for ALMaQUEST. **Left**: the sample is divided into the three morphological sub-samples in the panels in the figure as in Figure 10 and split within the barred panel into radial bar-flow classes (i.e. classes based on whether the galaxy's best-fit model included radial bar-flow). The median position, inner quartiles and span of the distributions are given by box plots in each of the three panels and the individual values given as markers. The markers are colour-coded by their SFR offset from the main-sequence (ΔMS). **Right**: histograms illustrating the concentration parameter for the un-barred sub-sample (grey "step" histogram) and the "barred + radial flow" and "barred + no radial flow" subsets (red and turquoise histograms respectively). The median position of each histogram is given by the white, red and turquoise dashed lines for the un-barred, "barred + radial flow" and "barred + no radial flow" distributions respectively. The 2-sided KS statistic and p-value are given in the plot to determine whether the "barred + radial flow" and "barred + no radial flow" distributions are drawn from the same distribution as that from the un-barred sub-sample. Both p-values here suggest that we cannot reject the null hypothesis and that the "barred + radial flow" subset is likely drawn from the same distribution as the un-barred sub-sample.

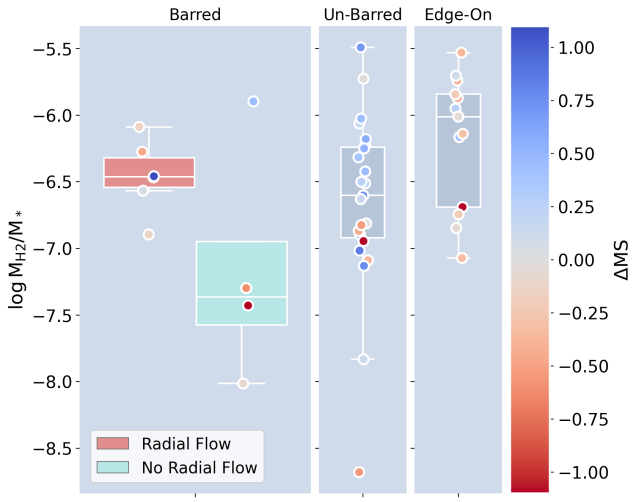

Figure 14. Figure illustrating the distribution of the molecular gas fraction (M_{H2}/M_*) in the central 1 kpc radius of ALMaQUEST galaxies using stellar mass maps from MaNGA (see Section 2.2.1). The sample is divided into the three morphological sub-samples in the panels in the figure as in previous figures and split within the barred panel into radial bar-flow classes (i.e. classes based on whether the galaxy's best-fit model included radial bar-flow). The median position, inner quartiles and span of the distributions are given by box plots in each of the three panels and the individual values given as markers. The markers are colour-coded by their SFR offset from the main-sequence (ΔMS).

tribution with those from the barred sub-sample's radial subsets (i.e. in the same manner as the corresponding plot in Figure 11). Again in this analysis, we find that the p-value for the distribution in the "barred + radial flow" subset < 0.05, suggesting we can reject the null hypothesis, while that for the "barred + no radial flow" subset » 0.05. This continues to suggest a similarity in the distributions of the "barred + no radial flow" subset and un-barred sub-sample, with the "barred + radial flow" subset appearing to be statistically distinct.

As addressed in Section 2.2.1, spatially resolved analysis of SFR in ALMaQUEST is limited by AGN-contamination or low S/N in the central regions of some of the galaxies in the sample. However, in Figures 14 & 15, we look at the molecular gas fraction and density within a central 1 kpc radius of each galaxy. In order to calculate the gas fraction ($\log M_{H2}/M_*$), we use stellar mass density maps from MaNGA (see Section 2.2.1). Using the same method detailed previously, we calculate the 2-sided KS statistic for the central gas fractions of the "barred + radial flow" and "barred + no radial flow" subsets shown in Figure 14 with those in the un-barred morphological sub-sample. We find that the p-value in both cases are > 0.05, suggesting that both barred radial bar-flow subsets have central gas fraction values drawn from the same distribution as the un-barred sub-sample. Using the same analysis, in the left panel of Figure 15, we show the distribution of molecular gas density ($\log \Sigma M_{H2}$) for ALMaQUEST. The median of the central gas density values for the "barred + radial flow" subset is clearly enhanced relative to the "barred + no radial flow" subset and un-barred sub-sample. Using the 2-sided KS statistic, we find that the null hypothesis can be rejected for the "barred + radial flow" subset, but not for the "barred + no radial flow", when compared to those in the un-barred sub-sample. This may imply that the centres of galaxies hosting radial bar-flows are generally more gas-rich.

In the right panel of Figure 15, we consider whether the variations in the signal-to-noise (SNR) of the ALMaQUEST molecular gas maps could explain the enhanced central gas density values observed in the "barred + radial flow" subset. We give more detail of this process in the Appendix, where we show that our results are robust against degrading all the original ALMaQUEST CO(1-

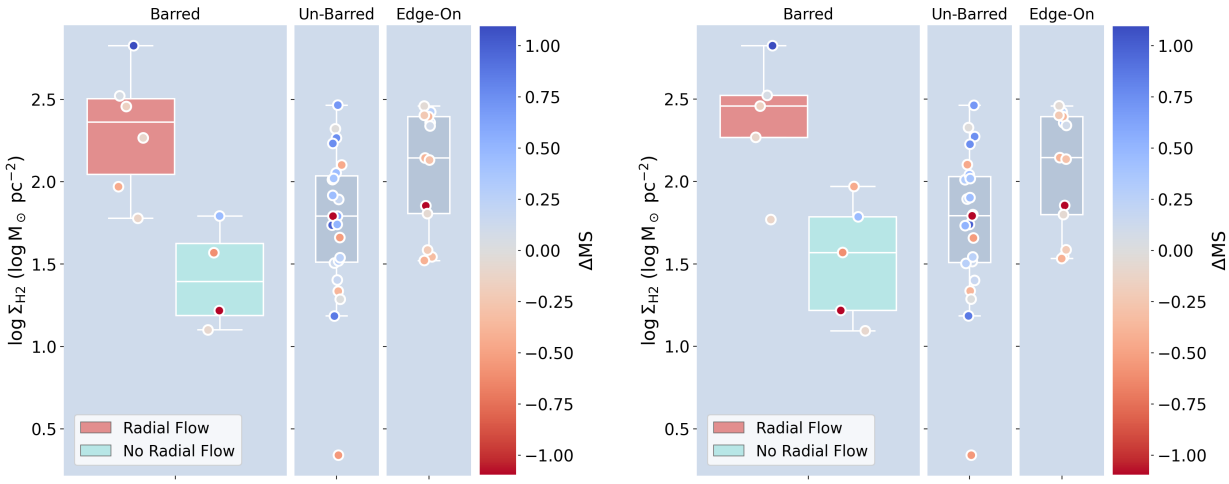

Figure 15. Figures illustrating the distribution of the molecular gas density (ΣM_{H2}) in the central 1 kpc radius of ALMaQUEST galaxies. **Left**: the sample is divided into the three morphological sub-samples in the panels in the figure as in previous figures and split within the barred panel into radial bar-flow classes. The median position, inner quartiles and span of the distributions are given by box plots in each of the three panels and the individual values given as markers. The markers are colour-coded by their SFR offset from the main-sequence (ΔMS). **Right**: the same as left but using radial bar-flow classes once we have degraded the ALMaQUEST cubes to have S/N < 30 (see text for detail).

0) datacubes to an SNR < 30. The right panel of Figure 15 shows the molecular gas density values when all ALMaQUEST datacubes have an SNR < 30. The main difference in this panel is that one object changes subset from the "barred + radial flow" subset to the "barred + no radial flow" subset when we use KinMS to re-model the degraded SNR datacubes. However, the median position of the central gas density values from the "barred + radial flow" subset remains higher than those in the "barred + no radial flow" subset and the results from the 2-sided KS test remain consistent with those calculated from the lefthand panel.

4 DISCUSSION

4.1 Features of radial bar-flow:

4.1.1 In barred galaxies

The primary question addressed in this work is whether there is a statistical relationship between the presence of an optical bar in a galaxy and the detection of non-circular kinematics of molecular gas (with a focus on radial bar-flow). We find that 60% of galaxies in ALMaQUEST that we classify as barred (see Section 2.3 for details of the classification system) also host radial molecular gas flow (see Section 3.1 for our definition of radial bar-flow). This is in comparison to the 30% and 38% in the un-barred and edge-on sub-samples respectively, which we illustrate in Figure 8 (where the edge-on sub-sample is composed of both barred and un-barred galaxies). We can infer from this that barred galaxies are statistically more likely to possess non-circular molecular gas kinematics that resembles radial bar-flow (i.e. gas moving in the plane of the galaxy as the result of the forcing frequency of a bar, Spekkens & Sellwood 2007). This finding echoes numerical simulations of molecular gas transport in barred galaxies, such as in Krumholz & Kruijssen (2015), where the role of large-scale galactic structures like bars are emphasised as critical drivers of gas dynamics and star-formation at the centre of galaxies. However, Kruijssen et al. (2014); Krumholz & Kruijssen (2015) also highlight the importance of timescale when observing radial gas dynamics. Their models cycle through distinct phases of accumulation, starburst, outflow and quenching, which results in a range of potential observations, depending on the phase in which the galaxy is observed. While radial bar-flow is more likely in our barred sub-sample, it follows, therefore, that it may not be present in all of our barred objects due to the effect of dynamical timescales.

In addition to the greater likelihood of radial bar-flow detection in our barred sub-sample, we also find that 90% of these objects are best fit by a 2-component surface brightness model (instead of a 1-component model; see Section 3.1 for details on the modelling process). Our un-barred and edge-on sub-samples are significantly less likely to be best-fit by 2-component surface brightness models, with 30% and 69% preferring a 2-component model over a 1-component model in these sub-samples respectively (see Figure 9). A multi-component surface brightness model can indicate the presence of a resonance system, where molecular gas is driven onto multiple resonant orbits by the pattern frequency of a bar or other axi-asymmetric feature (e.g. see Combes 1991; Comerón et al. 2014; Fraser-McKelvie et al. 2020; Chiba & Schönrich 2021). Strong resonant orbits occur at co-rotation and at the Lindblad resonances, where an orbit's epicyclic frequency is commensurate with the pattern frequency driven by the rotation of a central bar. Molecular gas rings have been directly observed in multiple previous studies, including Lu et al. (2022), where the authors find evidence of a molecular gas inflow along the bar of galaxy PGC34107, forming an asymmetric gas ring at the inner Lindblad resonance (ILR) using high-resolution millimeter interferometry from the *Northern Extended Millimeter Array* (NOEMA). We can infer, therefore, that a similar process may be underway in our barred sub-sample, whereby molecular gas is funneled along their bars into resonant orbits.

It is also noteworthy that the fraction of barred galaxies best-fit by 2-component surface brightness models is greater than the fraction in the "barred + radial flow" subset. As considered in Section 3.2, this difference can be predicted from the literature, which generally points to radial bar-flows caused by bar instabilities being transient compared to the lifetime of the bar itself. For example, Sormani et al. (2018); Sormani & Barnes (2019) infer from their simulations of the CMZ that the intrinsic morphological asymmetry of a galactic bar leads to intrinsically transient and time variable gas

inflows. Moreover, Schinnerer et al. (2023) study the inner 5 kpc of the local barred spiral galaxy NGC 1365 with *James Webb Space Telescope/Mid-Infrared Instrument* (JWST/MIRI) imaging alongside ALMA CO(2-1) mapping from PHANGS-ALMA (PHANGS: *Physics at High Angular resolution in Nearby GalaxieS*). They find asymmetric gas distributions along the bar lanes and a lop-sided star-formation distribution as well as evidence of streaming motions along the bar lanes. Using hydrodynamical simulations, they are able to replicate these observations, with transient streaming motions that occur within a dynamical time (which in the case of NGC 1365, is $\sim$ 30 Myr with streaming motion timescales as small as $\sim$ 6 Myr). Largely, this is attributed to the clumpiness of the gas distribution, which subsequently forms a highly variable inflow along the bar. Sormani et al. (2023) find very similar results when studying NGC 1097, which hosts gas inflow rates that vary over timescales of $\approx$ 10 Myr. Collectively, these studies strongly support a scenario of episodic gas accretion through short-lived radial inflows. When comparing these inflow timescales to the lifetime of a bar, the literature suggests that a bar can be stable over a period of 1-10 Gyr (e.g. Shen & Sellwood 2004; Gadotti & de Souza 2006; Gadotti & Coelho 2015; Cavanagh et al. 2022). It follows, therefore, that the long lifetime of the bar would maintain resonant structures within a galaxy on timescales that far exceed the lifetimes of transient radial flows. Consequently, it is more likely at any one time to observe a resonant gas structure than it is to observe a radial bar-flow in a barred galaxy, as we find in Section 3.2.

Another consistent property of the molecular gas in our barred sub-sample, especially the radial bar-flow subset, is a low concentration parameter (defined as $r_{50,CO}/r_{50,r}$ in Section 3.3 and illustrated in Figure 13). We find a narrower range of concentration parameter values for this subset of galaxies at the low end of the distribution, suggesting that the gas in these objects is concentrated relative to to the un-barred and edge-on sub-samples. The range of values is also narrower than that measured for the objects in the barred sub-sample without radial bar-flow detection. However, the small size of this subset makes the comparison somewhat tenuous. This result is consistent with the findings of Yu et al. (2022), who use a sample of similar size drawn from EDGE-CALIFA (EDGE: *Extragalactic Database for Galaxy Evolution*; CALIFA: *Calar Alto Legacy Integral Field Area*) to assess the correlation between central molecular gas concentration and large-scale galaxy asymmetry. In particular, the authors focus on the difference in gas concentrations between galaxies with and without an optical bar, but do not find a statistically significant difference between the concentration parameters they calculate for these two sub-samples. This is despite the fact that their barred distribution peaking at higher gas concentrations compared to their un-barred distribution. Our results illustrated in Figure 13 present a similar scenario, where the concentration parameters for our barred sub-sample do peak at a lower value than the distribution drawn from the un-barred and edge-on sub-samples, but are not drawn from a different distribution according to the 2-sided KS statistic. Ultimately, more data is required to assess this result, but in the context of the high fraction of resonant gas structures found in our barred sub-sample, it follows that this gas would be more centrally concentrated along these inner orbits (e.g. see Sakamoto et al. 1999; Jogee et al. 2005; Kuno et al. 2007; Combes et al. 2014).

We also find a notable consistency in some of the dynamical properties of the radial bar-flow in our barred sub-sample. In Figure 10, we show that all the objects in our "barred + radial flow" subset have a ratio of radial to transverse bar-flow velocities ($\overline{V}_r$ / $\overline{V}_t$) $\lesssim$ 1 (see Section 3.2 for more details). This is in comparison to both the un-barred and edge-on radial bar-flow subsets, which have a larger scatter of $\overline{V}_r$ / $\overline{V}_t$. $\overline{V}_r$ / $\overline{V}_t$ << 1 suggesting an essentially circular orbit, while $\overline{V}_r$ / $\overline{V}_t$ >> 1 implies significant non-circular motion. Spekkens & Sellwood (2007) also comment on the relevance of the $\overline{V}_r$ / $\overline{V}_t$ ratio, finding that their bisymmetric model produces $\overline{V}_r$ / $\overline{V}_t$ = 1 for solid body rotation and $\overline{V}_r$ / $\overline{V}_t$ $\approx$ 0.67 for flat rotation. All of the objects in our "barred + radial flow" subset have $R_b > R_{\rm turn}$, meaning that their bars extend beyond the rising portion of their rotation curves (i.e. where there is solid body rotation). As our $\overline{V}_r$ and $\overline{V}_t$ parameters are a fixed value in the region R_b, we are effectively averaging these velocities over the rising and flat portions of their rotation curves. Values of $\overline{V}_r$ / $\overline{V}_t$ $\lesssim$ 1 for our "barred + radial flow" subset appear, therefore, to be in the range anticipated by Spekkens & Sellwood (2007) for distortions created by the presence of a bar. It is, however, possible that our radial-bar flow model is capturing shocks induced along molecular ridges (i.e. long structures along the leading edge of a bar) in our barred sub-sample, which can rapidly decelerate molecular gas and potentially alter our $\overline{V}_r$ and $\overline{V}_t$ parameters (e.g. Kuno et al. 2000). In the case of our un-barred and edge-on sub-samples, where $\overline{V}_r$ / $\overline{V}_t$ >> 1 fall outside the values anticipated by Spekkens & Sellwood (2007), reinforcing our argument that the flows modelling in these objects are, at least in part, kinematically distinct from those in the barred sub-sample.

The transverse velocity component of the bar flow should not in principle be related to the rotation velocity resulting from the stellar potential. We investigate this in Figure 16, where we show that there is no statistically significant correlation (with p-values>> 0.05) between the transverse velocity component and either the total stellar mass or rotation velocity. Our measured transverse velocity components, therefore, do not seem connected to the stellar potential and can be viewed as a distinct feature of the gas flow in our objects. This result once again implies that there is a kinematic similarity in how cold gas is moving in our barred sub-sample, compounding the evidence that they are undergoing the same process; drawing gas onto resonant orbits corresponding to the forcing frequency of a bar. While it is not possible to distinguish between gas inflows and outflows in the plane of the disc using our bisymmetric radial bar-flow model, in the context of the enhanced central molecular gas density in our "barred + radial flow" subset, the preponderance of resonant inner orbits in these objects and our comparisons to the literature in this discussion, we are inclined to infer that we are observing radial bar inflows as opposed to outflows.

4.1.2 *In un-barred galaxies*

While the focus of this paper is the molecular gas kinematics of galaxies hosting an optical bar, we also find some compelling results for our un-barred sub-sample. Only 30% of un-barred galaxies are best modelled with radial bar-flow and the majority use a 1-component surface brightness model to describe the spatial distribution of their molecular gas (70%, see Section 3.2). When comparing these findings with those from the barred sub-sample, we can infer that these objects are kinematically distinct. Moreover, the results from Figure 13 further compound this inference by illustrating the wide range of concentration parameters in the un-barred sub-sample and the higher median of the distribution. Once again we can defer to Yu et al. (2022) for a potential explanation for the wide range of concentration parameters that we measure. The authors find a correlation between the strength of non-axisymmetric structure and central molecular gas concentration, where axi-asymmetric structures can be due to a bar or the presence of spiral arms. They suggest

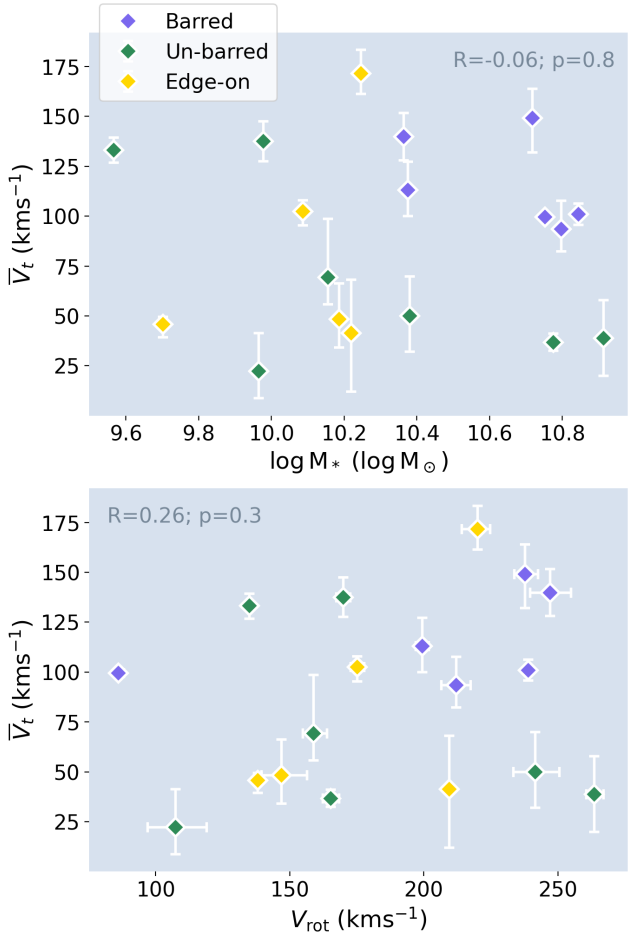

Figure 16. Figures exploring the dependence of the transverse velocity component ($\overline{V}_t$) in our radial bar-flow subsets. **Top**: plot of $\overline{V}_t$ against stellar mass (M_*). We calculate the Spearman correlation coefficient and find p − value >> 0.05. We, therefore, infer that these quantities are not correlated. **Bottom**: plot of V_t against rotation velocity (V_{rot}). We calculate the Spearman correlation coefficient and find p − value >> 0.05, again suggesting there is no correlation between these quantities.

that instead of there being a distinct difference between the gas dynamics in barred and un-barred galaxies, that the dynamics are a function of asymmetry, with a unified mechanism. This is further supported by Géron et al. (2021, 2023), who extend this idea to different bar types, suggesting that there is a continuum of bar types; more specifically that there is no bifurcation between weak and strong bar in terms of the effect on their host galaxy. Our un-barred sub-sample likely contains galaxies with a range of structural asymmetries, corresponding to a range of pattern strengths with which to drive gas inwards. Géron et al. (2021, 2023) & Walmsley et al. (2022) also note that weak bars are under-detected in GZ2, with the barred sub-sample preferring strong bars. While our barred sub-sample is dominated by strong bars, the un-barred sub-sample is likely to contain a fraction of weakly barred galaxies. It is also possible that this sub-sample contains galaxies under-going minor mergers or interactions, which can also act to centralise the molecular gas distribution (e.g. Eliche-Moral et al. 2011).

4.2 Do radial bar-flows affect SFE in barred galaxies?

In Section 3.3, we investigate the second goal of this paper, which is to look for correlations between non-circular gas kinematics and the SFE of galaxies in our barred sub-sample. We define a quantity $\log(\mathrm{SFE_{measured}}) - \log(\mathrm{SFE_{expected}})$ (see Section 3.3 for detailed definition) to measure enhancement/suppression in a galaxy's global SFE relative to the offset in SFE we would expect given its place on the star-forming main-sequence (and the median global SFE of ALMaQUEST objects within the scatter of main-sequence). In Figure 11, we illustrate the distribution of this quantity for each of our morphological sub-samples and radial subsets. Notably, we see an indication that the SFE offset quantity in the "barred + radial flow" subset is suppressed relative to the values measured in the un-barred sub-sample and "barred + no radial flow" subset. This result could imply that our "barred + radial flow" subset has suppressed total SFE relative to that expected from their position relative to the main-sequence. Echoing the distributions in Figure 13, we also see a broader range of values in the un-barred sub-sample, which could again be explained by the likelihood that this sub-sample is composed of a variety of galaxy morphologies, as argued in Section 4.1.2. In order to investigate Figure 11 further, in Figure 12 we plot the distribution of $\log(\mathrm{SFE_{H\alpha,measured}}) - \log(\mathrm{SFE_{expected}})$ calculated in the discs of ALMaQUEST galaxies, derived from MaNGA optical IFS (see Section 2.2.1). We find a similar distribution to that in Figure 11 in terms of the relative enhancement/suppression between the morphological sub-samples and radial flow subsets. Again, our interpretation of this result is limited by the size of the respective samples, but finding a comparable result by an independent method does add credence to our interpretation of SFE-suppression in the "barred + radial flow" subset. Extending this interpretation with Figure 12, the suppression of SFE in the disc regions of objects in the "barred + radial flow" subset could be seen in the context of the "compaction scenario" (Tacchella et al. 2016) as evidence of the disc being quenched by the inward radial flow of molecular gas. However, larger-scale analysis dividing barred galaxies into subsets depending on radial bar-flow detection is required to substantiate this argument.

In the literature, there is a general link between a galaxy being quenched and a higher stellar density (ΣM_*) in its central 1 kpc radius (e.g. Fang et al. 2013; Woo et al. 2015; Davis et al. 2022). We assess this connection in Figure 17 and find that our barred sub-sample has a higher median central ΣM_* compared to the other morphological sub-samples. Furthermore, all the central ΣM_* values in the "barred + radial flow" subset lie above $\approx 8.25\ \mathrm{M_\odot pc^{-2}}$, whereas the un-barred and edge-on sub-samples, as well as the "barred + no radial flow" subset, all have density values extending below that threshold. Once again, this suggests a similarity between the "barred + radial flow" subset. It also is consistent with the literature given that our most SFE-suppressed subset also has consistently high central ΣM_*, suggesting that a growth in central stellar density may be a signal of galactic quenching.

It is widely theorised that molecular gas is depleted or expelled after large-scale starburst activity and exhausted in bulge-dominated early-type galaxies (e.g. Gavazzi et al. 2015; Zolotov et al. 2015; Tacchella et al. 2016; Spinoso et al. 2017). However, in Davis et al. (2014); French et al. (2015); Davis et al. (2016), this scenario is contradicted, with the authors finding higher than expected gas fractions ($\log M_{H2}/M_*$) in early-type galaxies. Furthermore, Lin et al. (2022) report in their analysis of Green Valley galaxies in ALMaQUEST that quenching is driven by the combination of reduced $\log M_{H2}/M_*$ and suppressed SFE, challenging the picture that star-formation is

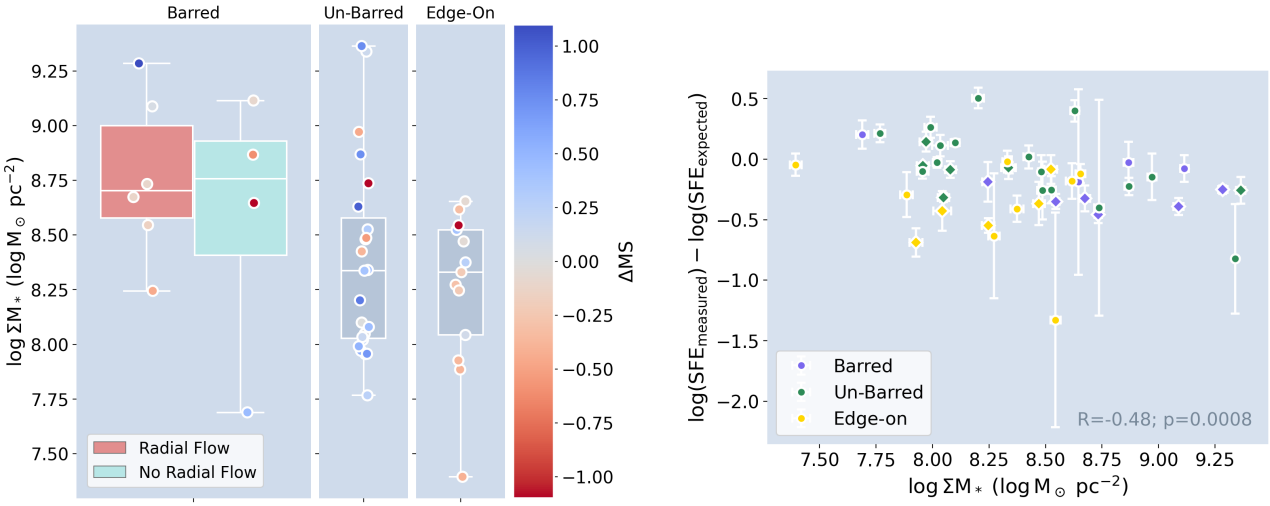

Figure 17. Figures illustrating the distribution of the stellar density (ΣM_*) in the central 1 kpc radius of ALMaQUEST galaxies. **Left**: the sample is divided into the three morphological sub-samples in the panels in the figure as in Figure 10 and split within each panel into radial bar-flow subsets. The median position, inner quartiles and span of the distributions are given by box plots in each of the three panels and the individual values given as markers. The markers are colour-coded by their SFR offset from the main-sequence (ΔMS). **Right**: Relationship between $\log(\mathrm{SFE_{measured}}) - \log(\mathrm{SFE_{expected}})$ and central stellar density. Each marker is colour-coded by which morphological sub-sample the galaxy belongs to and the median trend of the markers is overlaid by the grey line. Objects in the radial bar-flow subset are illustrated with a diamond-shaped marker. We calculate the Spearman correlation coefficient as $R = -0.5$ with a $p - \mathrm{value} << 0.05$, suggesting our $\log(\mathrm{SFE_{measured}}) - \log(\mathrm{SFE_{expected}})$ quantity and central stellar density are negatively correlated in ALMaQUEST.

quenched purely by gas depletion. In Figure 14, we look at the distribution of molecular gas fraction in a 1 kpc central aperture for the "barred + radial flow" subset relative to those drawn from the un-barred sub-sample. The "barred + radial flow" subset, despite having suppressed SFE, does not appear to have a depleted central molecular gas reservoir, with the median central molecular gas fraction for the "barred + radial flow" subset roughly coincident with that of the un-barred sub-sample (and enhanced compared to the "barred + no radial flow" subset). We conduct the same analysis using total molecular gas fraction values and find a similar result. Moreover, in Figure 15 we measure a higher median central molecular gas surface density in the "barred + radial flow" subset, consistent with Figure 13 (i.e. in agreement with their centralised gas distributions). Using the 2-sided KS statistic, we find that the central density values in the "barred + radial flow" subset are drawn from a different distribution than those in the un-barred sub-sample. Visually, it appears that the "barred + radial flow" subset is drawn from the higher density end of the un-barred distribution and the "barred + no radial flow" subset the lower end. We can infer from the higher central median density of the "barred + radial flow" subset, that molecular gas depletion is not the driver of SFR-suppression in our "barred + radial flow" subset. This result is also supported by Figure 12, from which we tentatively argue that the suppressed median value of the disc SFE measurement in the "barred + radial flow" distribution could be caused by inward radial bar-flow drawing gas away from the disc, effectively leading to quenched star-formation. Radial bar-flow of molecular gas appears to centralise the gas reservoir in these objects, but does not fuel an enhancement in SFR (i.e. in both the global and disc measurements; we attempt to conduct a similar analysis for the central 1 kpc in the Appendix). In our un-barred sub-sample, however, the galaxies with similarly high central gas densities have significantly higher ΔMS values compared to those in the "barred + radial flow" subset. This supports the argument that the presence of a bar is responsible for the SFE-suppression instead of central gas depletion in these objects.

In order to explain the apparent relative suppression of SFE measurements in our "barred + radial flow" subset, we may require a more dynamical prescription of quenching. Dynamically-driven shear and the stability of the central gas reservoir against collapse contribute to a morphological picture of quenching ("Morphological Quenching", Martig et al. 2009). For example, Davis et al. (2014); Gensior et al. (2020) discuss the role of gas dynamics on SFE-suppression in Early-Type Galaxies (ETGs), in which the majority of the molecular gas reservoir is concentrated in the rising portion of a galaxy's rotation curve, where shear is generally higher. Although our barred sub-sample are clearly morphologically distinct from ETGs, the "barred + radial flow" subset does contain consistently centralised molecular gas reservoirs, implying that this gas is also restricted to a high-shear region of the host galaxy's rotation curve. Furthermore, the presence of radial flow will also contribute to shear, particularly in the central area where most of the gas is concentrated. The presence of strong shear could also increase the velocity dispersion of cold gas clouds by actively pulling them apart, increasing the Toomre Q parameter (Toomre 1964). This is corroborated by the studies of M51 by Meidt et al. (2013a,b), who detect a clear anti-correlation between strong gas flows and star formation (traced by Hα and 24 μm emission). This implies a direct connection between the star-forming ability of GMCs and their dynamical environment; suggesting that GMCs embedded in the vicinity of radial streaming motions are significantly stabilised against gravitational collapse. These findings contribute to a scenario where our "barred + radial flow" galaxies have driven gas inwards (via the instabilities induced by a bar) towards a central molecular gas reservoir that is largely gravitationally stable. This is in comparison to our "barred + no radial flow" subset, which is less centrally concentrated and obviously does not have the contribution to shear provided by the radial flow. As discussed in Section 4.1.1, these objects are potentially at different dynamical stage of their evolution; for example, prior to the radial inflow of gas or after a central starburst once the central molecular gas reservoir gravitationally destabilises. As de-

picted in Figures 11 & 13, our most concentrated objects are largely quenched, where SF is restricted to the central region and maybe also be subject to dynamical suppression.

While there are multiple studies in the literature that find a connection between galaxies hosting bulges and SFE-suppression (e.g. Saintonge et al. 2012; Martig et al. 2013; Davis et al. 2014), the influence of bars on the star-forming potential of galaxies is less consistent. Wang et al. (2012) summarises the variety of results in this field, finding that the galaxies in their sample with strong bars either have enhanced central star-formation rates or star-formation that is suppressed. Resolved studies find that SFE can vary along a bar and between galaxies; e.g. Maeda et al. (2023) finds star-formation generally suppressed along bars, but enhanced at the bar-ends, while Díaz-García et al. (2021) finds no evidence of SFE variation between the bar and bar-ends, but significant variation between galaxies. These differences may be explained to some extent by bar/bar-end definition in the case of resolved studies, but the variety of results may also indicate that galaxies classed as barred in these studies contain a mixture of objects dominated by different mechanisms or at different stage of their evolution. Our identification of radial bar-flow may provide a method to sub-divide barred galaxies into subsets with similar global properties based on the large-scale dynamics of their molecular gas. We suggest that this sub-division of optically barred galaxies potentially captures the portion of objects with suppressed SFE in the literature. Without making the distinction, many studies find little difference in the star-formation efficiency of barred galaxies when comparing them to their un-barred counterparts (e.g. Saintonge et al. 2012). To assess this result further, a larger sample of galaxies with CO data of comparable resolution and sensitivity to the data in ALMaQUEST would be required.

5 SUMMARY & CONCLUSIONS

In this work, we investigate the statistical relationship between the presence of an optical bar and radial molecular gas flows and, furthermore, whether that connection influences the star formation activity of the host galaxies. We use CO(1-0) maps of 46 galaxies in the ALMaQUEST survey to create 3D kinematic models (using the KinMS package), from which we infer whether or not there is evidence of radial gas motion. In tandem with our dynamical analysis of the molecular gas in this sample, we also create morphological classes (i.e. barred, un-barred and edge-on) based on optical classifications from Galaxy Zoo and HyperLEDA. By combining our morphological sub-samples with our radial bar-flow classifications, we find the following key results:

- We find a bar fraction of 0.30 for the ALMaQUEST sample using our classification procedure outlined in Figure 2.
- In Figure 8, we show that 60% of the barred sub-sample are classed as having radial bar-flow, compared to 30% and 38% in the un-barred and edge-on sub-samples respectively. This suggests that gas flows resembling radial bar-flows are more common in galaxies hosting axi-asymmetric features like bars.
- 90% of our barred sub-sample have a multi-component surface brightness profile as the best-fit model to their molecular gas distribution (see Figure 9). This is likely indicative of a resonant ring structure driven by bar-instabilities. We also find a greater proportion of our barred sub-sample have multi-component surface brightness profiles compared to the fraction of those found to host radial bar-flows. This supports a scenario where gas inflows are transient compared to the timescale over which a galactic bar is stable.
- Comparing the radial and transverse velocity components ($\overline{V}_r$ & $\overline{V}_t$) of the radial bar-flow used in our model (defined in Section 3.1), in Figure 10 we find that our barred sub-sample have $\overline{V}_r$ / $\overline{V}_t \lesssim 1$, but see a much wider spread of $\overline{V}_r$ / $\overline{V}_t$ ratios in our other morphological sub-samples. This not only implies a dynamical similarity in terms of the molecular gas kinematics in our barred objects, but also suggests that the gas is moving inwards in a tighter "spiral motion" in these objects.
- The objects in our "barred + radial flow" subset appear to have suppressed SFE compared to those in the "barred + no radial flow" subset and in the un-barred sub-sample (both globally using GSWLC-X2 and WISE values and in their discs using MaNGA IFS; see Figures 11 & 12). The ability to make this distinction, through molecular gas kinematics, goes some way in explaining the tension between various results in the literature regarding SFE-enhancement/suppression in barred galaxies.
- Galaxies in our "barred + radial flow" subset have consistently concentrated molecular gas distributions compared to the other subsets, which all have a wider spread of concentration parameters (see Figure 13). Again, we interpret this as an indication that the galaxies in the "barred + radial flow" subset are undergoing a similar kinematic process, wherein gas is driven inwards.
- In Figure 14, we show that the objects in the "barred + radial flow" subset are not depleted of molecular gas relative to the other subsets when comparing their respective central gas fractions. This subset also has a higher median molecular gas density in their inner 1 kpc compared to the "barred + no radial flow" subset (see Figure 15), suggesting that radial bar-flow may act to centralise gas in these galaxies. Exhaustion of the central molecular gas reservoir is, therefore, not the reason for the SFR-suppression observed in this subset. We speculate that dynamical effects, such as shear, driven by the radial motion of gas may act to quench the centralised gas reservoir.

In conclusion, we find that barred galaxies more likely to host radial molecular gas flows, and that the presence of those flows can also alter their large-scale properties, notably their star-forming efficiency and the central compaction of their molecular gas reservoir. Despite the molecular gas being more centrally concentrated in barred galaxies with detected radial bar-flow, it does not power a central SFR enhancement (at least, not while the flow is on-going). Conversely, we find these galaxies appear to have suppressed SFE both globally and in their discs. From this, we can begin to infer that gas is being drawn inwards, quenching the discs of these galaxies, and increasing the central molecular gas density. However, the dynamics of the flows themselves may act to stabilise the molecular gas against fragmentation and collapse (e.g. through effects like shear), suppressing the subsequent SFE of the gas.

To further this work, a larger survey of galaxies with high spatial and spectral resolution CO mapping with high sensitivity is required, as to-date these surveys have been limited in size. The resolution and sensitivity of the data is critical for meaningful kinematic modelling, which we propose is a vital tool for understanding the baryon cycle and its impact on the evolution of barred galaxies.

ACKNOWLEDGEMENTS

LMH and AS acknowledge support from the Royal Society. TAD acknowledges support from the UK Science and Technology Facilities Council through grants ST/S00033X/1 and ST/W000830/1. This paper makes use ALMA data from project S/JAO.ALMA#2011.0.01234.S. ALMA is a partnership of ESO (representing its member states), NSF (USA) and NINS (Japan), together with NRC (Canada), MOST and ASIAA (Taiwan), and KASI (Republic of Korea), in cooperation with the Republic of Chile. The Joint ALMA Observatory is operated by ESO, AUI/NRAO and NAOJ.

LL acknowledges support from NSTC through grants MOST 108-2628-M-001-001-MY3 and NSTC 111-2112-M-001-044-. HAP acknowledges support by the National Science and Technology Council of Taiwan under grant 110-2112-M-032-020-MY3.

This project makes use of the MaNGA-Pipe3D dataproducts. We thank the IA-UNAM MaNGA team for creating this catalogue, and the Conacyt Project CB-285080 for supporting them.

DATA AVAILABILITY

All ALMaQUEST data products used in this work are available in the ALMA science archive (https://almascience.eso.org/asax/). MaNGA IFS and stellar mass maps are also publicly available in the SDSS Science Archive Server (SAS; https://dr17.sdss.org/sas/). GALEX and WISE data can be acquired from their respective online databases (i.e. https://salims.pages.iu.edu/gswlc/ and http://vizier.cds.unistra.fr/ respectively). The NSA data used in this paper can be accessed via the SDSS DR17 website (https://www.sdss4.org/dr17/manga/manga-data/catalogs/#DRPALLFile).

REFERENCES

Baldwin J. A., Phillips M. M., Terlevich R., 1981, PASP, 93, 5
Bertin G., 2014, Dynamics of Galaxies, 2 edn. Cambridge University Press, doi:10.1017/CBO9780511731990
Blanton M. R., Roweis S., 2007, AJ, 133, 734
Blanton M. R., Kazin E., Muna D., Weaver B. A., Price-Whelan A., 2011, AJ, 142, 31
Bundy K., et al., 2015, ApJ, 798, 7
Cardelli J. A., Clayton G. C., Mathis J. S., 1989, ApJ, 345, 245
Cavanagh M. K., Bekki K., Groves B. A., Pfeffer J., 2022, MNRAS, 510, 5164
Chabrier G., 2003, PASP, 115, 763
Chiba R., Schönrich R., 2021, MNRAS, 505, 2412
Chown R., et al., 2019, MNRAS, 484, 5192
Coelho P., Gadotti D. A., 2011, ApJ, 743, L13
Combes F., 1991, in Combes F., Casoli F., eds, Vol. 146, Dynamics of Galaxies and Their Molecular Cloud Distributions. p. 255
Combes F., 2001, in Funes J. G., Corsini E. M., eds, Astronomical Society of the Pacific Conference Series Vol. 230, Galaxy Disks and Disk Galaxies. pp 213–220 (arXiv:astro-ph/0008341), doi:10.48550/arXiv.astro-ph/0008341
Combes F., et al., 2014, A&A, 565, A97
Comerón S., et al., 2014, A&A, 562, A121
Cutri R. M., et al., 2021, VizieR Online Data Catalog, p. II/328
Davis T. A., et al., 2013, Monthly Notices of the Royal Astronomical Society, 429, 534
Davis T. A., et al., 2014, MNRAS, 444, 3427
Davis T. A., Greene J., Ma C.-P., Pandya V., Blakeslee J. P., McConnell N., Thomas J., 2016, MNRAS, 455, 214
Davis T. A., et al., 2018, MNRAS, 473, 3818
Davis T. A., Zabel N., Dawson J. M., 2020, KinMS: Three-dimensional kinematic modelling of arbitrary gas distributions (ascl:2006.003)
Davis T. A., et al., 2022, arXiv e-prints, p. arXiv:2203.01358
Díaz-García S., et al., 2021, A&A, 654, A135
Egusa F., Hirota A., Baba J., Muraoka K., 2018, ApJ, 854, 90
Eliche-Moral M. C., González-García A. C., Balcells M., Aguerri J. A. L., Gallego J., Zamorano J., Prieto M., 2011, A&A, 533, A104
Ellison S. L., Nair P., Patton D. R., Scudder J. M., Mendel J. T., Simard L., 2011, MNRAS, 416, 2182
Ellison S. L., Lin L., Thorp M. D., Pan H.-A., Scudder J. M., Sánchez S. F., Bluck A. F. L., Maiolino R., 2021, MNRAS, 501, 4777
Fang J. J., Faber S. M., Koo D. C., Dekel A., 2013, ApJ, 776, 63
Fraser-McKelvie A., et al., 2020, MNRAS, 495, 4158
French K. D., Yang Y., Zabludoff A., Narayanan D., Shirley Y., Walter F., Smith J.-D., Tremonti C. A., 2015, ApJ, 801, 1
Gadotti D. A., Coelho P., 2015, Highlights of Astronomy, 16, 339
Gadotti D. A., de Souza R. E., 2006, ApJS, 163, 270
Gavazzi G., et al., 2015, A&A, 580, A116
Gensior J., Kruijssen J. M. D., Keller B. W., 2020, MNRAS, 495, 199
Géron T., Smethurst R. J., Lintott C., Kruk S., Masters K. L., Simmons B., Stark D. V., 2021, MNRAS, 507, 4389
Géron T., et al., 2023, MNRAS, 521, 1775
Heitsch F., Slyz A. D., Devriendt J. E. G., Burkert A., 2006, MNRAS, 373, 1379
Hogarth L. M., Saintonge A., Davis T. A., 2023, MNRAS, 518, 13
Janowiecki S., Catinella B., Cortese L., Saintonge A., Brown T., Wang J., 2017, MNRAS, 466, 4795
Jarrett T. H., et al., 2013, AJ, 145, 6
Jogee S., Scoville N., Kenney J. D. P., 2005, ApJ, 630, 837
Kauffmann G., et al., 2003, MNRAS, 341, 54
Kennicutt Jr. R. C., 1998, ARA&A, 36, 189
Kruijssen J. M. D., Longmore S. N., Elmegreen B. G., Murray N., Bally J., Testi L., Kennicutt R. C., 2014, MNRAS, 440, 3370
Krumholz M. R., Kruijssen J. M. D., 2015, MNRAS, 453, 739
Kuno N., Nishiyama K., Nakai N., Sorai K., Vila-Vilaró B., Handa T., 2000, PASJ, 52, 775
Kuno N., et al., 2007, PASJ, 59, 117
Lelli F., Davis T. A., Bureau M., Cappellari M., Liu L., Ruffa I., Smith M. D., Williams T. G., 2022, MNRAS, 516, 4066
Lin L., et al., 2020, ApJ, 903, 145
Lin L., et al., 2022, ApJ, 926, 175
López-Cobá C., Sánchez S. F., Lin L., Anderson J. P., Lin K.-Y., Cruz-González I., Galbany L., Barrera-Ballesteros J. K., 2022, ApJ, 939, 40
Lu S., et al., 2022, The Astrophysical Journal, 927, 215
Maeda F., 2023, IAU Symposium, 373, 207
Maeda F., Ohta K., Fujimoto Y., Habe A., Ushio K., 2020, MNRAS, 495, 3840
Maeda F., Egusa F., Ohta K., Fujimoto Y., Habe A., 2023, ApJ, 943, 7
Makarov D., Prugniel P., Terekhova N., Courtois H., Vauglin I., 2014, A&A, 570, A13
Martig M., Bournaud F., Teyssier R., Dekel A., 2009, ApJ, 707, 250
Martig M., et al., 2013, MNRAS, 432, 1914
Masters K. L., et al., 2011, MNRAS, 411, 2026
Meidt S. E., et al., 2013a, in Wong T., Ott J., eds, Vol. 292, Molecular Gas, Dust, and Star Formation in Galaxies. pp 139–142, doi:10.1017/S174392131300080X
Meidt S. E., et al., 2013b, ApJ, 779, 45
Meidt S. E., et al., 2020, ApJ, 892, 73
Nair P. B., Abraham R. G., 2010, VizieR Online Data Catalog, p. J/ApJS/186/427
Olsson E., Aalto S., Thomasson M., Beswick R., 2010, A&A, 513, A11
Pettini M., Pagel B. E. J., 2004, MNRAS, 348, L59
Saintonge A., Catinella B., 2022, ARA&A, 60, 319
Saintonge A., Tacconi L. J., Fabello S., Wang J., Catinella B., et al. 2012, ApJ, 758, 73

Saintonge A., Catinella B., Cortese L., Genzel R., Giovanelli R., et al. 2016, MNRAS, 462, 1749
Sakamoto K., Okumura S. K., Ishizuki S., Scoville N. Z., 1999, ApJ, 525, 691
Salak D., Tomiyasu Y., Nakai N., Kuno N., Miyamoto Y., Kaneko H., 2017, ApJ, 849, 90
Salim S., et al., 2016, ApJS, 227, 2
Salim S., Boquien M., Lee J. C., 2018, ApJ, 859, 11
Sánchez S. F., et al., 2016, Rev. Mex. Astron. Astrofis., 52, 171
Sánchez S. F., et al., 2018, Rev. Mex. Astron. Astrofis., 54, 217
Sánchez S. F., et al., 2022, The Astrophysical Journal Supplement Series, 262, 36
Schinnerer E., et al., 2023, ApJ, 944, L15
Shen J., Sellwood J. A., 2004, ApJ, 604, 614
Shlosman I., Frank J., Begelman M. C., 1989, Nature, 338, 45
Sormani M. C., Barnes A. T., 2019, MNRAS, 484, 1213
Sormani M. C., Binney J., Magorrian J., 2015, MNRAS, 454, 1818
Sormani M. C., Treß R. G., Ridley M., Glover S. C. O., Klessen R. S., Binney J., Magorrian J., Smith R., 2018, MNRAS, 475, 2383
Sormani M. C., et al., 2023, MNRAS, 523, 2918
Spekkens K., Sellwood J. A., 2007, ApJ, 664, 204
Spinoso D., Bonoli S., Dotti M., Mayer L., Madau P., Bellovary J., 2017, MNRAS, 465, 3729
Tacchella S., Dekel A., Carollo C. M., Ceverino D., DeGraf C., Lapiner S., Mandelker N., Primack Joel R., 2016, MNRAS, 457, 2790
Toomre A., 1964, ApJ, 139, 1217
Topal S., Bureau M., Davis T. A., Krips M., Young L. M., Crocker A. F., 2016, MNRAS, 463, 4121
Walmsley M., et al., 2022, MNRAS, 509, 3966
Wang J., et al., 2012, MNRAS, 423, 3486
Watanabe Y., Sorai K., Kuno N., Habe A., 2011, MNRAS, 411, 1409
Willett K. W., et al., 2013, MNRAS, 435, 2835
Woo J., Dekel A., Faber S. M., Koo D. C., 2015, MNRAS, 448, 237
Wright E. L., et al., 2010, AJ, 140, 1868
Yu S.-Y., et al., 2022, A&A, 666, A175
Zolotov A., et al., 2015, MNRAS, 450, 2327
de Vaucouleurs G., de Vaucouleurs A., Corwin H. G. J., Buta R. J., Paturel G., Fouque P., 1991, Sky & Telesc., 82, 621

APPENDIX A: CENTRAL SFE DERIVED FROM MANGA

In Figure A1, we illustrate differences in $\mathrm{SFE}_{\mathrm{H}\alpha,\mathrm{measured}} - \mathrm{SFE}_{\mathrm{expected}}$ between our morphological sub-samples and radial flow subsets in the central 1 kpc. As previously stated, this analysis is limited by the number of spaxels masked in the central region of objects in ALMaQUEST. We, therefore, use the median SFE spaxel value in this region, using the MaNGA SFR maps and ALMaQUEST M_{H2} maps re-binned to the MaNGA spaxel grid.

APPENDIX B: SNR DEGRADATION (ONLINE-ONLY)

We test for variations in the SNR in ALMaQUEST datacubes by degrading all cubes with an SNR > 30 to below this threshold. SNR≈30 is the median value of the SNR for objects in the un-barred sub-sample. We degrade these cubes by creating 2D images of randomly generated values drawn from a Gaussian distribution with a width equal to the standard deviation of the original noise of the cube. We smooth these 2D noise images with the beam and then add them to each channel of the original datacubes (i.e. each 2D noise image is created independently for each channel). The new SNR of the degraded cube is then calculated and if it is still > 30, we create 2D noise images with integer multiples of the original cube standard deviation and repeat the process, with increasingly higher multiples of the noise, until its SNR < 30.

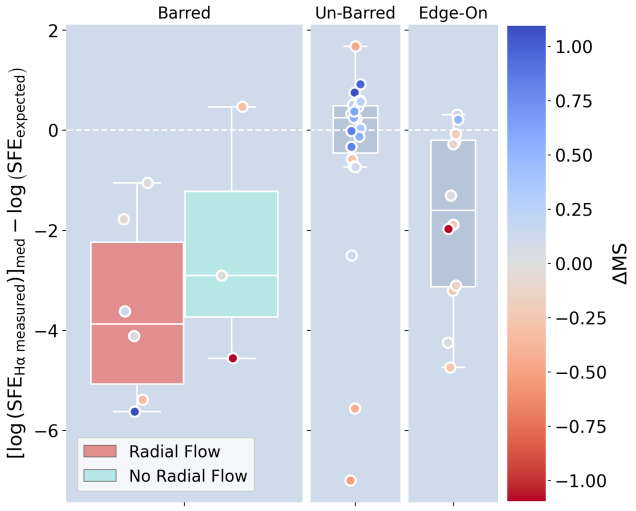

Figure A1. The distribution of the $\mathrm{SFE}_{\mathrm{H}\alpha,\mathrm{measured}} - \mathrm{SFE}_{\mathrm{expected}}$ quantity in the central region of ALMaQUEST objects using Hα emission from MaNGA. For each object, we sum SFR and M_{H2} spaxels within the central 1 kpc.

Our degraded datacubes are re-modelled using KinMS, replicating the process. This produces a new distribution of best-fit surface brightness profiles and a new radial bar-flow subset. The fraction of galaxies for each morphological sub-sample with radial bar-flow is presented in Figure A2 alongside the fraction with 2-component surface brightness models. The fraction of barred galaxies with radial bar-flow is 0.50, compared to 0.04 and 0.08 for the un-barred and edge-on sub-samples respectively. The fraction of barred galaxies with 2-component models is 0.80, compared to 0.17 and 0.54 for the un-barred and edge-on sub-samples respectively.

The SNR of the datacubes, therefore, does affect the detection of radial bar-flow and the best-fit model. However, it does not affect our conclusions. Figure B1 illustrates this further by showing the suppression of SFE in the "barred + radial flow" subset relative to the "barred + no radial flow" subset, replicating our original interpretation. We infer, therefore, that our results and conclusions are robust against SNR variations in the ALMaQUEST data.

This paper has been typeset from a TEX/LATEX file prepared by the author.

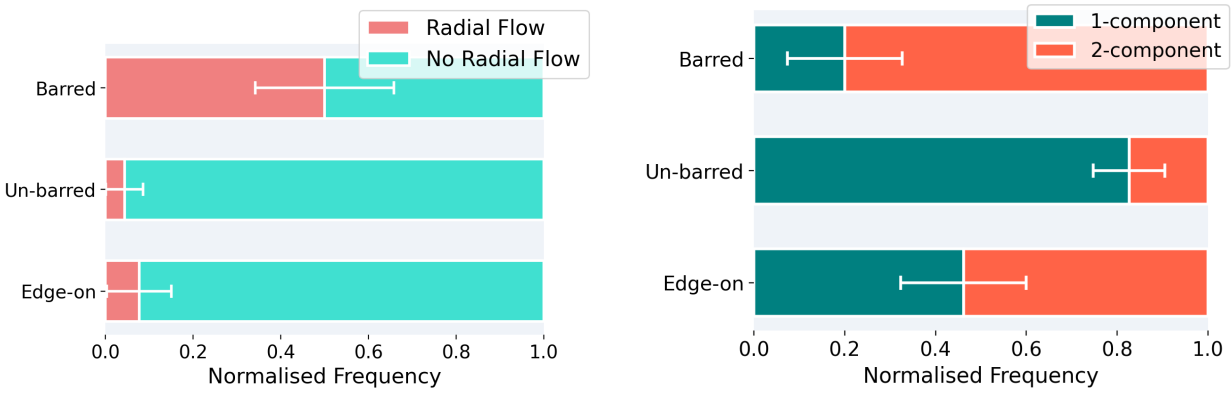

Figure A2. Figures 8 (left) & 9 (right) re-plotting using KinMS models created using our SNR-degraded datacubes.

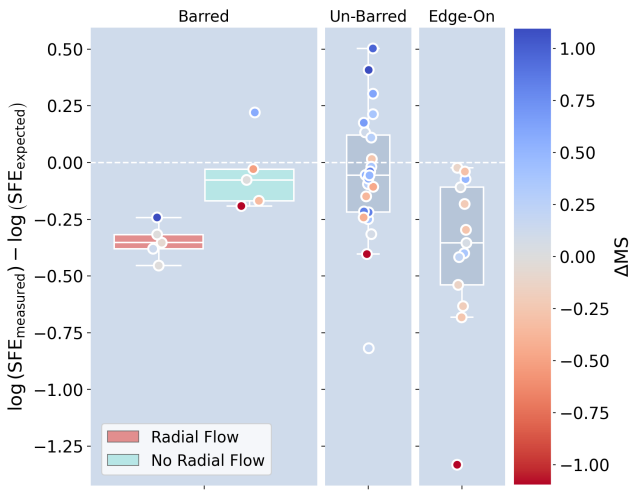

Figure B1. Figure 11 re-plotted using our SNR-degraded datacubes and KinMS models.